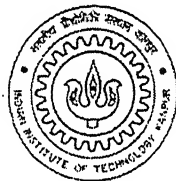


# Finite Element Simulation of Deep Drawing Process Using Solid Element

A Thesis Submitted for  
partial fulfillment of Requirements for the Degree of  
Master of Technology

by

T.S.Sudhish Kumar



to the

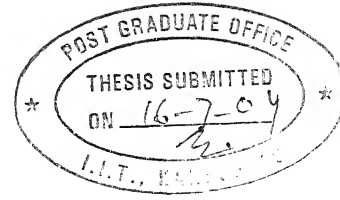
DEPARTMENT OF MECHANICAL ENGINEERING  
INDIAN INSTITUTE OF TECHNOLOGY KANPUR

25 OCT 2004  
द्रुषोत्तम का शीनाय केलकर पुस्तकालय  
भारतीय प्रौद्योगिकी संस्थान कानपुर  
प्रदापि क्र० A.....149280.....

TH  
17/10/2004/01  
K. 206 f



A149280



# Certificate

It is certified that the work contained in the thesis entitled "*Finite Element Simulation of Deep Drawing Process Using Solid Element*", has been carried out under my supervision and that this work has not been submitted elsewhere for a degree.

Dr. P. M. Dixit

July, 2004.

Department of Mechanical Engineering,

I.I.T. Kanpur.

# Abstract

In the present work, a three-dimensional large deformation elasto-plastic finite element code has been developed for the analysis of deep drawing process. The parametric study is presented to show the effects of two process parameters namely sheet thickness and material properties.

The updated Lagrangian formulation is used to develop the finite element equations using 8-noded solid element. The new incremental objective stress measure and logarithmic strain measure are used which allow the use of large incremental displacement. Modified Newton-Raphson iterative technique is used to solve the nonlinear incremental equations. The material is assumed to be elastic-plastic strain hardening yielding according to the von Mises criterion. The strain hardening behavior is modeled by a power law. Due to small accelerations, inertial forces are not included. The body forces are also neglected. The friction is assumed to be of sticking type at the punch-sheet interface, while the die-sheet and the blankholder-sheet interfaces are assumed to have sliding friction. To reduce the storage and computational time, the skyline method of assembly and the static condensation of coefficient matrix are carried out.

Validation of the code is done by comparing the predicted finite element results with available experimental results. Parametric study shows that the punch force increases with the increase in sheet thickness. The thickness strain is observed to be the highest in the clearance region while the equivalent stress is found to be the largest at the punch corner zone.

# Acknowledgements

I wish to express my deep sense of gratitude and indebtedness to my thesis supervisor **Dr.P.M.Dixit** who bestowed upon me his confidence and patience during this dissertation. His able guidance and invaluable thoughts were the foremost to help me complete this thesis.

I would also like to place my gratitude to **Mr. Ravindra Kumar Saxena** whose constant encouragement helped me to come out of difficult times.

I would also take this as the opportunity to thank **Mr. Abhijit Mahato** and **Mr. Sachin Singh Gautam** whose help I frequently sought throughout this dissertation.

I am thankful to **Abhijit, Anoop, Anupam, Bijoy, Deepak, Kisun, Prasad, Prince, Pritham, Soumya, and Shrikant** whose friendship I wish to cherish for life. I am also grateful to my friends **Arvind, Vikram** and all others who made my stay in IITK a memorable one.

Lastly, I would thank My Family to be with me and help me complete my dream of studying in IIT Kanpur.

T.S. Sudhish Kumar

IIT Kanpur

22 July 2004

*To my Father.*

# Contents

Certificate	i
Abstract	ii
Acknowledgements	iii
Contents	iii
List of Figures	vii
List of Symbols	viii
<b>1 Introduction</b>	<b>1</b>
1.1 Literature Review . . . . .	2
1.1.1 Finite Element Method . . . . .	4
1.1.2 Blankholder Force and Blank Design . . . . .	6
1.1.3 Anisotropy . . . . .	7
1.2 Objective . . . . .	8
1.3 Structure of Present Work . . . . .	9
<b>2 Mathematical Modeling of Large Deformation Elasto-Plastic Problem</b>	<b>10</b>
2.1 Updated Lagrangian Formulation . . . . .	10
2.2 Kinematics of Finite Deformation . . . . .	11

2.3	Stress Measures . . . . .	12
2.4	Strain Measures . . . . .	15
2.5	Elastic Constitutive Equation . . . . .	16
2.6	Elasto-Plastic Constitutive Equation . . . . .	16
2.7	Incremental Updated Lagrangian Formulation . . . . .	20
2.8	Boundary Conditions for 3-D Deep Drawing of Rectangular Sheet . .	22
2.8.1	Initial Boundary Conditions . . . . .	23
2.8.1.1	The Sheet-Punch Interface . . . . .	23
2.8.1.2	The Free Surfaces . . . . .	24
2.8.1.3	X-Z Plane of Symmetry . . . . .	24
2.8.1.4	Y-Z Plane of Symmetry . . . . .	25
2.8.1.5	Sheet-Die Interface . . . . .	25
2.8.1.6	Surface with Blank-Holding Force . . . . .	26
2.8.2	Incremental Boundary Conditions . . . . .	26
2.8.2.1	Recognition of State of Nodes . . . . .	26
2.8.2.2	Punch Penetration and Specified Displacement . . .	26
2.8.2.3	Die Penetration and Specified Displacement . . . . .	27
<b>3</b>	<b>Finite Element Formulation</b>	<b>30</b>
3.1	Matrix Notation . . . . .	30
3.2	Finite Element Equations . . . . .	32
3.3	Static Condensation Scheme . . . . .	36
3.4	Determination of Stresses . . . . .	38
3.5	Integration of the Constitutive Equation . . . . .	38
3.6	Solution Procedure . . . . .	40
3.6.1	Contact Algorithm . . . . .	41
3.6.2	Modified Newton - Raphson Scheme . . . . .	42



3.6.3	Numerical Integration Scheme . . . . .	43
3.6.4	Divergence Handling Procedures . . . . .	43
<b>4</b>	<b>Results and Discussion</b>	<b>45</b>
4.1	Validation . . . . .	46
4.2	Thickness Strain Distribution . . . . .	48
4.3	Deformed Mesh . . . . .	49
4.4	Stress Distribution . . . . .	51
4.5	Parametric Study . . . . .	51
4.5.1	Effect of Sheet Thickness . . . . .	52
4.5.2	Effect of Material Properties . . . . .	53
<b>5</b>	<b>Conclusions and Scope for Future Work</b>	<b>55</b>
	<b>References</b>	<b>57</b>

# List of Figures

1.1	Deep Drawing Process . . . . .	1
2.1	Deformation of a domain . . . . .	11
2.2	Fixed and Material Frames of references. . . . .	14
2.3	The complete domain of the Problem. . . . .	23
2.4	The domain considered for analysis. . . . .	24
2.5	Subdivision of domain. . . . .	27
2.6	Penetration of node in the punch region. . . . .	28
2.7	Penetration of node in the die region. . . . .	29
4.1	The Descretised Sheet . . . . .	45
4.2	The variation of punch load with punch displacement . . . . .	46
4.3	Thickness Strain of the sheet metal along the x axis . . . . .	48
4.4	The deformed sheet metal . . . . .	49
4.5	The complete plate showing ear formation at the corner . . . . .	50
4.6	The Stress distibution in the domain . . . . .	51
4.7	The variation of punch load with sheet thickness . . . . .	52
4.8	The variation of thicknes strain with sheet thickness . . . . .	53
4.9	The variation of punch load with material . . . . .	54
4.10	The variation of thicknes strain with material . . . . .	54

# List of Symbols

$\Psi$	Yield Function.
$\{a\}$	Flow vector.
$[B_L]$	Linear strain displacement matrix.
$[B_N]$	Non-linear strain displacement matrix.
$C^E$	Fourth order elasticity tensor.
$C^{EP}$	Fourth order elastic-plastic tensor.
$[C^E]$	Elasticity matrix.
$[C^{EP}]$	Elasto-plastic matrix.
$e, e_{ij}$	Green-Lagrange strain tensor, component.
$E$	Young's modulus.
$f(), F()$	Generic representation of functions.
$F_x$	Component of force in x direction.
$F_y$	Component of force in y direction.
$F_z$	Component of force in z direction.
$f_i$	Surface force component.
$\{f\}$	Global internal force vector.
$\mathbf{F}, F_{ij}$	Deformation gradient tensor, component.
$[F]$	Matrix representation of Deformation gradient tensor.
$\{F_1\}$	External force vector corresponding to nodes of type 1.
$\{F_2\}$	External force vector corresponding to nodes of type 2.
$\{\hat{F}\}$	Condensed form of global external force vector.
$\{F\}$	Global external force vector.
$\{R\}$	Unbalance force vector.
$\{\hat{R}\}$	Condensed form of unbalance force vector.

$K$	Hardening coefficient
$[K]$	Stiffness matrix.
$[K_L]$	Linear part of stiffness matrix.
$[K_N]$	Non linear part of stiffness matrix.
$[\widehat{K}]$	Condensed form of stiffness matrix.
$t_x$	Traction in x direction.
$t_y$	Traction in y direction.
$t_z$	Traction in z direction.
$n$	Hardening exponent.
$N_i$	Shape function.
$\{P\}$	Basic load vector.
$[Q], Q_{ij}$	Transformation matrix, component.
$\mathbf{R}, R_{ij}$	Rotation tensor, component.
$[R]$	Matrix representation of components of $R$ .
$\mathbf{S}, S_{ij}$	Second piola-Kirchoff stress tensor, component.
$[S]$	Matrix representation of components of $S$ .
$S_f$	Surface with traction applied.
$tol_e$	Tolerance for convergence of the numerical method.
$\{u_1\}$	Displacement vector corresponding to nodes of type 1.
$\{u_2\}$	Displacement vector corresponding to nodes of type 2.
$\{u\}$	Total displacement vector.
$\{\hat{u}\}$	Condensed form of displacement vector.
$\{\Delta u^I\}$	Displacement vector due to basic load vector.
$\{\Delta u^{II}\}$	Displacement vector due to unbalanced force vector.
$\mathbf{U}, U_{ij}$	Right stretch tensor, component.
$[U]$	Matrix of Right stretch tensor.
$[U''], U''_{ij}$	Matrix representation of the components of $U$ with respect to principal axes, component.

$V$	Volume.
$\mathbf{W}, W_{ij}$	Spin tensor, component.
$x_i$	Co-ordinate of a generic particle.
$\delta$	Variation.
$\delta_{ij}$	Kronecker delta.
$\Delta$	Increment in quantity.
$\boldsymbol{\varepsilon}, \varepsilon_{ij}$	Small strain tensor, component.
$[\boldsymbol{\varepsilon}]$	Matrix representation of $\boldsymbol{\varepsilon}$ .
$\varepsilon_{pq}^p$	Equivalent plastic strain.
$[\boldsymbol{\varepsilon}^L], \varepsilon_{ij}^L$	Matrix representation of the components of logarithmic strain tensor with respect to principal axes, component.
$\boldsymbol{\varepsilon}^{pl}, \varepsilon_{ij}^{pl}$	Plastic part of $[\boldsymbol{\varepsilon}^L]$ , component.
$\boldsymbol{\eta}, \eta_{ij}$	Non-linear part of the Green-Lagrange strain tensor, component.
$\lambda_i$	Principal stretch component.
$\lambda, \mu$	Lame's constants.
$\nu$	Poisson's ratio.
$\rho$	Density.
$\boldsymbol{\sigma}, \sigma_{ij}$	Cauchy stress tensor, component.
$[\boldsymbol{\sigma}]$	Matrix representation of $\boldsymbol{\sigma}$ .
$\dot{\boldsymbol{\sigma}}, \dot{\sigma}$	Cauchy stress rate tensor, component.
$\overset{\circ}{\boldsymbol{\sigma}}, \overset{\circ}{\sigma}_{ij}$	Jaumann stress rate tensor, component.
$\sigma_y$	Yield stress.
$[\boldsymbol{\sigma}^M], \sigma_{ij}^M$	Matrix representation of the components of the stress tensor with respect to a material frame, component.
$\boldsymbol{\sigma}', \sigma'_{ij}$	Deviatoric part of the Cauchy stress tensor, component.
$\{\Phi_i\}$	Array of shape functions.

# Chapter 1

## Introduction

Sheet metal parts are one of the predominant commodity in different engineering applications. Manufacturing of sheet metal parts by means of press working is a cost effective process since it eliminates expensive machining and welding operations giving better quality finished product and it enables to produce components at a very high rate. Among the manufacturing of these sheet metal parts, deep drawing is an extensively used press working process.

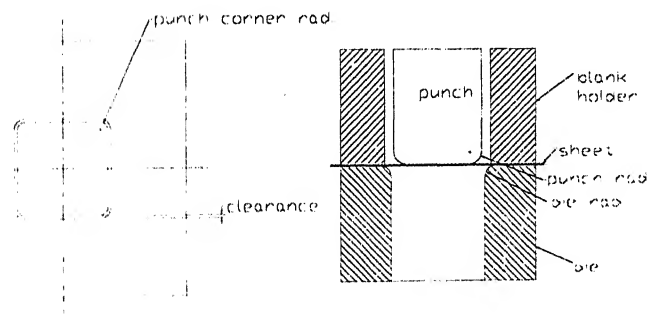


Figure 1.1: Deep Drawing Process

Deep drawing is a process in which a blank or work piece, usually controlled by a pressure plate, is forced into and/or through a die by means of a punch to form a

hollow component [1]. The procedure with greatest range of application is the deep drawing with rigid tooling, involving draw punches, a blankholder and a female die. The blank is pulled over the draw punch into the die, the blankholder prevents any wrinkling taking place in the flange [2]. The schematic diagram of the process is shown in figure (1.1). Deep drawing without a blankholder is carried out only if the part does not tend to wrinkle, i.e. it is thick or has small amount of deformation [3]. The workpiece is subjected to radial tension forces and tangential compressive forces. Therefore, the material is compressed in the tangential direction and stretched in the radial direction.

Deep drawing of non circular components finds applications in many industries, such as construction, automobile manufacturing, aerospace technology, and electrical equipments. However, the stress and strain behaviors exhibited in non-circular deep drawing processes are so complicated that the mechanics of deformation differs very appreciably from that observed in circular deep drawing process. Among the non circular deep drawing processes, box drawing is the most basic process. A major problem in box drawing is the difference of metal flow rates between the straight walls and the corners of the deforming part. This will result in an uneven material distribution around the cup wall. In addition, the variable flow rates may also cause wrinkles in the flange of the drawn cup.

## 1.1 Literature Review

The development of reliable analytical procedures to predict the deformation and stress fields in sheet-metal forming processes is a possible solution to make the process more efficient. However, this development has encountered serious obstacles. The major cause is the presence of various non-linearities such as

- the geometric non-linearity due to large deformation of the readily pliable sheet,
- the material non-linearity due to the deformation going into plastic range, and
- the kinematic non-linearity due to the contact of sheet metal with punch and die along with friction at the contacting surfaces.

Modeling of these non-linearities is a difficult task due to the complexities involved in the underlying mathematics and the numerical instabilities that come up during the solution

stage.

In the past, a number of approximate methods of analysis viz., the slab method, the slip line field method, the visio-plasticity method, the upper and lower bound techniques and the Hill's general method, have been developed for various forming processes [4]. In the slab method, the workpiece being deformed is divided into several slabs. For each slab, simplifying assumptions are made with respect to stress distributions. The resulting approximate equilibrium equations are solved with imposition of stress compatibility between slabs and boundary tractions. The solution of these equations gives approximate load requirement and stress distribution in the forming process. The slip-line field method is used in plane strain problems for perfect plastic materials and uses the hyperbolic properties of the stress equations. The construction of slip-line fields, although produces an "exact" stress distribution, has limitation in predicting results comparable with experimental work. From the stress distributions, velocity fields can be calculated through plasticity equations. The visio-plasticity method combines experimental and analytical methods. After the velocity vectors are determined from an actual test, strain-rates are calculated and the stress distributions are obtained from plasticity equations. The method has helped to obtain reliable solutions for the processes where the experimental determination of velocity vectors was possible. The upper-bound method requires the guessing of admissible velocity fields, among which the best one is chosen by minimizing total energy. Information leading to a good selection of velocity fields come from experimental evidence and experience. This method, with experience, can deliver a fast and relatively accurate prediction of loads and velocity distributions. Hill has given a general method of analysis for metal-working processes when the plastic flow is unconstrained. The method is based on a criterion of approximation derived from the interpretation of the virtual work-rate principle.

The above methods have been useful in predicting the forming loads and overall geometry changes of deforming workpieces with approximation. However, accurate determination of the effects of various process parameters on the detailed metal flow has become possible with the use of finite element methods. This method is sufficiently versatile to handle various geometries, materials and boundary conditions, hence widely used in the analysis of sheet metal forming.



### 1.1.1 Finite Element Method

In the simulation of sheet metal forming, several finite element models such as membrane, shell and solid (3-D) models have been proposed. The membrane model is the simplest one. Toh and Kobayashi [5] modeled the square cup drawing process based on finite strain formulation and membrane theory. An optimum blank shape was determined based on finite element results of net material flow. But they assumed zero blankholder force in the computations. Saran and Samulesson [6] modeled the behavior of sheet materials by a triangular membrane constant strain element. They used hypoelastic-viscoplastic material model including Hill's plastic anisotropy, power law hardening and strain rate sensitivity. They demonstrated that, a huge reduction in the number of elements can be achieved by adaptive re-meshing. Majlessi and Lee [7] developed a finite element analysis technique using elements with membrane characteristics. They ignored the effects of bending and unbending and found approximate solution to the problem of nonaxisymmetric deep drawing. However, the membrane formulation neglects stress variation in thickness and considers the stress components only in the plane of sheet. Thus, it is not appropriate to employ the membrane theory for conditions in which bending deformation of sheets becomes significant and dominant like in deep drawing. In general, the processes where the bending effect is significant are simulated by the shell model or the solid model.

Onate and Saracibar [8] presented the viscous voided shell approach for developing the bending/membrane finite element formulation for sheet metal forming. These viscous voided shell elements can be selectively used for membrane or full bending analysis of the sheet according to the nature of deformation. They concluded that for 3D cases, using complex punches and dies, this approach is effective and economical. Chou et al. [9] simulated the sheet metal forming by plane-strain shell elements using the stress resultant theory. This theory is based on quadratic yield function, a hardening rule, and the associated flow rule. Shu et al. [10] introduced a new finite element approach for the direct prediction of blank shapes and strain distributions for desired final shapes in sheet metal forming, based on a one-step simulation algorithm. They have given new and compact formulations of the DKT<sup>1</sup> shell element. Although the shell model is more effective than the solid model, it still takes a substantial amount of computational time and memory space for its integration in the thickness direction. Chou et al. [12] proposed a stress resultant constitutive law based on the orthotropic yield function of

---

<sup>1</sup>Discrete Kirchhoff Triangular (DKT) shell element, is widely employed in non-linear static and dynamic analysis [11].

Hill for sheets with planar isotropy. They avoided integration through-the-thickness by considering a plate element, and showed a substantial amount of saving in computational time.

Keck et al. [13] modeled the deep drawing of rectangular blanks using eight noded hexahedrals. They assumed a constant gap blankholder force in the analysis, but in practice the blankholder force is given by the die cushion. Lei et al. [14] modeled an elasto-plastic finite element solution based on solid element and finite-strain plasticity for a free bending and a square cup drawing process. The law of constant friction is assumed at the die-workpiece interface and the coefficient of friction remains constant during the process. They investigated the punchload, metal flow, stress distribution and springback quantitatively. They have shown that for small initial workpieces, it is better to use a circular blank shape, and for large initial workpieces, an optimum blank shape is more desirable. Kaiping et al. [15] simulated the square-cup-deep drawing using an 8-node 3-D brick element with one integration point which is a mixed element based on the Hu-Washizu principle with hourglass control, and a 4-node quadrangular 3-D shallow shell element with six degrees of freedom per node [16]. They showed that for the same mesh and the same simulation the 8-node 3-D mixed elements have consummated much less CPU time and used less loading steps than the 4-node 3-D shallow shell elements. Thus in some applications, the shell elements might be replaced by 8-node 3-D mixed elements without losing much precision and with more economically. Explicit finite element technique is a dynamic procedure employing the central difference method. The advantage of this technique is that, there is no need to solve the system of equations and therefore, considerable smaller CPU time is needed, as compared to implicit technique. Manalis et al. [17] simulated the square cup deep drawing process using the explicit non-linear finite element code DYNA-3D. Error estimation and mesh enrichment procedures are necessary to define accurately the current shape of the sheet for the simulation of complex forming process. Bonet [18] showed that these procedures can be efficiently implemented in existing finite element software with negligible overheads. But, they did not consider derefinement and removal of nodes from regions exhibiting small errors which is essential for the processes like deep drawing. Fine die details like sharp corners can not be simulated with the above techniques. Menezes and Teodosiu [19] have published a deep drawing simulation of solid model using 8-noded brick elements using augmented Lagrangian method. Their formulation was based on Jaumann stress tensor and Green-Lagrange strain tensor. They however did not present the variation on punch load and displacement and also were unable to validate the thickness strain with that of the experimental result. They reported that although larger computational resource

was needed for solid elements the deformation obtained was more realistic. The number of elements required to give results for solid element were also lesser in comparison to shell elements.

### 1.1.2 Blankholder Force and Blank Design

Blankholder force plays an important role in the deep drawing process since it controls the material flow into the die cavity. The predominant failure modes in deep drawing process are wrinkling and fracture. In many cases these defects can be eliminated by appropriate control of blankholder force. Osakada et al. [20] proposed a method for determining an optimal blankholder force which does not cause wrinkling and localized thinning. In this method they used a control algorithm to the FEM program which controls the blankholder force depending on wrinkling, thinning, indentation and thickening. Ahmetoglu et al. [21] conducted experiments on an aluminum alloy and arrived at blankholder profile as a function of stroke that prevents wrinkling and fracture. Lorenzo et al. [22] proposed the optimal blankholder force path which permits to obtain the maximum height component avoiding both wrinkling and tearing. They have suggested a closed-loop control system based on the fuzzy reasoning interfaced with a FEM code. The control system interacts with the numerical simulation, carries out a continuous monitoring of some relevant process variables like draw-in, punch force, blankholder lifting-up and suggests the most effective adjustment of the blankholder force according to the implemented knowledge.

Blank design is a critical part in the deep drawing process. Inverse approach is a method to determine the position of the material points in the initial blank from the corresponding material points on the final product. Guo et al. [23] presented the inverse approach to evaluate the large plastic strains of tridimensional metallic sheets obtained by deep drawing process. They used triangular membrane element and deformation theory of plasticity. Backward tracing is a key concept to trace backward from the final desirable configuration to an intermediate preform or initial blank. Ku et al. [24] applied the backward tracing scheme of the rigid-plastic finite element method to the three-dimensional blank design of sheet metal forming. They concluded that sound products can be obtained using backward tracing without any machining after forming. Kim and Huh [25] also applied inverse finite element approach to multistage deep drawing process to determine the optimum blank shape from the desired final shape. The analysis results suggest that the intermediate die shapes and punch radius should be changed to get the

optimum final shape with uniform thickness distribution. Colgan and Monaghan [26] tried to determine the most important factors influencing a drawing process, utilizing the help of a design of experiments and statistical analysis. The FEA program AutoForm was used to model the cup formation. They made the ANOVA<sup>2</sup> table which, for a given analysis, helps, to determine, which of the factors need control and which do not [27]. By their work they have shown that the main aspect that the ANOVA highlighted is that the geometry of the tooling is generally most important, especially the die radius. But more work need to be done to refine the model and to quantify friction values for the punch side and die side of the blank.

### 1.1.3 Anisotropy

Most sheet metals exhibit anisotropic behavior in their deformation. Anisotropy in sheet metals comes in mostly due to cold working especially during its rolling. The quadratic yield criterion by Hill [28] has been the most popular choice to represent the anisotropy of sheets, particularly for steel. His yield criterion was suitable for rolled sheets, which exhibited orthotropic symmetry. The Hill's yield criterion and its variants were comfortably applied to steel and other metals having FCC or BCC type of crystallographic structure, but, had anomalous behavior toward highly ductile materials such as aluminum. Yoon et al. [29] cite how this anomalous behavior led many researchers to develop other types of yield criteria. Hu and Wang [30] describe a selection procedure for various anisotropic factors and give an insight on the anisotropic characteristics of materials in various metal forming processes. Several non-quadratic yield criteria were later developed by Hershey [31], Gotoh [32], Banabic et al. [33] and Itskov and Askel [34] etc to simulate the anisotropy in sheet metals. In most of these yield criteria the equivalent stress was calculated using Cauchy stress and its deviatoric part and anisotropy was later provided to the yield function. Each criterion thus developed has its own merits for specific applications.

An extension of von Mises yield criterion was proposed by Hershey [31] for polycrystals and later generalized by Hosford [35]. This Yield function makes it possible to represent yield surface between Mises and Tresca.

An important extension of this yield function to anisotropic materials was done by

---

<sup>2</sup>The ANOVA is the statistical treatment most commonly applied to the results of the experiment to determine the percent contribution of each factor.

Barlat et al. [36] which later became popular as Barlat's yield criterion. They provided anisotropy to the stress values in different directions and made the yield function an intrinsic function of these factors by utilizing the modified stress deviator instead of deviatoric portion of Cauchy stress. Karafillis and Boyce [37] later proposed a modification to this yield criterion and defined the effective stress to be a weighted sum of two yield criteria. Banabic et al. [33] developed a non-quadratic yield criterion for orthotropic sheet metals assuming plane-stress conditions. Their yield criterion was a variation of Barlat's. Yoon et al. [29] presented in their review, a variation of Barlat's yield criterion for 2D sheet deformation. Barlat et al. [38] improved upon this and determined the anisotropic factors for a few of the metal alloys in their paper. Bron and Besson [39] gave another factor for anisotropy in Barlat's yield criterion and also proved for the first time the convexity of the yield criterion. They developed a optimization function to determine the anisotropic factors applied to the yield function. They also developed an algorithm to implement the Barlat's yield criterion to 3D finite element formulation.

The deep drawing process is one particular sheet forming operation on which several researchers have tried these yield functions. The Hill's yield function has been applied to deep drawing process for shell, degenerated solid elements and solid element by Kawka and Makinouchi [40], Wu [41] Menezes and Teodosiu [19] and others. Barlat's yield criterion has been widely used for deep drawing process especially for shell and membrane elements because of its superlative quality in simulating deep drawing in comparison with Hill's yield criterion. Yoon et al. [42], Bron and Besson [39] and Nakamachi [43] are some of them.

## 1.2 Objective

The objective of the present work is to develop a 3-D large deformation elasto-plastic finite element code for the analysis of deep drawing process. The updated Lagrangian formulation, that is convenient for handling material and geometric nonlinearities, is used. The new incremental objective stress measure and logarithmic strain measure are used instead of the Jaumann stress rate and Green-Lagrange nonlinear strain measures used in most of the literature. Modified Newton-Raphson iterative technique is used to solve the nonlinear incremental equations. To minimize the storage, skyline method of assembly is used. Static condensation scheme is employed to reduce the computational time.

The material is assumed to be elastic-plastic strain hardening and yielding according to von Mises yield criterion. The effects of temperature and strain rate (viscoplasticity effects) on the yield strength of the material are ignored in this work. The inclusion of these effects renders the analysis quite complex. Due to small accelerations, inertial forces are not included. The punch and die are assumed rigid. The friction is assumed to be sticking type at the punch-sheet interface, and sliding at the die-sheet interface. The blank holding force is applied incrementally assuming to reach the total at the end of all increments.

First, the code is validated by comparing predicted values of punch force with experimental results of reference [5]. Next, a parametric study of punch force and thickness strain is carried out to show the effects of process variables namely sheet thickness and anisotropy.

### 1.3 Structure of Present Work

The thesis is organized as follows.

In the second chapter, the mathematical modeling of the deep drawing process is presented. The boundary condition applied to the given problem is also presented here.

In the third chapter, the finite element formulation and the numerical scheme are presented.

In the fourth chapter, the validation and the results for a typical case are presented. It also includes a discussion on the parametric study.

Conclusions and suggestions for further work are presented in chapter five.

## Chapter 2

# Mathematical Modeling of Large Deformation Elasto-Plastic Problem

In this chapter, mathematical model of a static large deformation elasto-plastic problem is developed. The description of motion, stress measures, strain measures and constitutive laws used in the formulation of the governing equations for static large deformation elasto-plastic problems are presented.

### 2.1 Updated Lagrangian Formulation

In the study of the deformation of a body subjected to external loading, often the original undeformed and unstressed state of the body is used for the formulation of its equation of motion. This is known as Lagrangian formulation. This formulation is convenient for small deformation, which is the case in many engineering problems. In such cases, the deformed configuration does not deviate much from the original one and hence the deformation can be described by an infinitesimal strain tensor, for which the strain-displacement relations are linear. On the other hand, for large deformation problems, one has to use a finite strain measure, which is expressed by a nonlinear strain-displacement relation. Furthermore, the equations of motion when expressed in the reference configuration depend on the deformation. Hence, for large deformation problems, the Lagrangian formulation proves to be cumbersome with the governing equations being difficult to solve. In such cases, one solves the problem using an incremental method known as updated

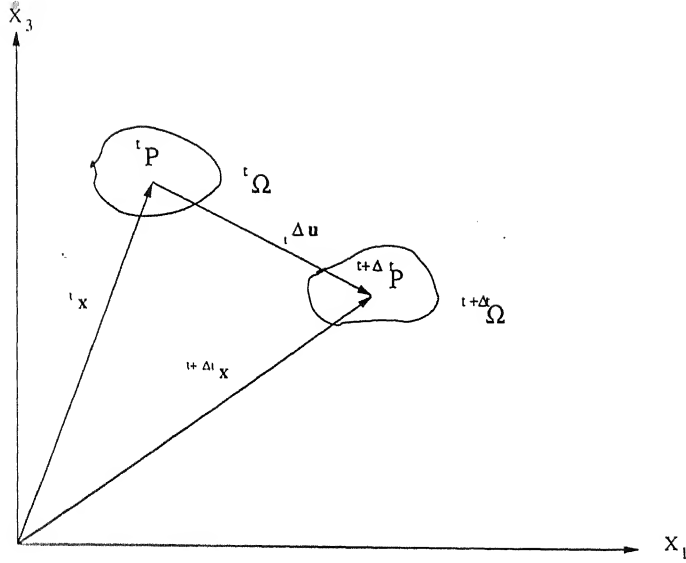


Figure 2.1: Deformation of a domain

Lagrangian formulation. In this formulation, it is assumed that the states of stress and deformation of the body are known till the current configuration, say at time  $t$ . The main objective is then to determine the incremental deformation and stresses during the time step  $\Delta t$ , i.e from time  $t$  to  $t + \Delta t$ . Here, the current configuration is used as the reference configuration for obtaining the incremental values. Unlike in the Lagrangian formulation, an incremental strain tensor is used. This methodology is particularly useful for elasto-plastic materials because the stress-strain relationship in such materials is usually expressed in an incremental fashion.

## 2.2 Kinematics of Finite Deformation

Consider a domain  ${}^t\Omega$  at time  $t$  with respect to a given global coordinate system  $\mathbf{X}_i$  as shown in the figure 2.1. Let this body deform to domain  ${}^{t+\Delta t}\Omega$ . Let the position vector corresponding to any particle  $P$  be  ${}^t\mathbf{x}_i$  at time  $t$  and  ${}^{t+\Delta t}\mathbf{x}_i$  at time  $t + \Delta t$  with relative displacement vector as  ${}^t\Delta\mathbf{u}_i$ . The relative displacement gradient tensor at time  $t + \Delta t$  is therefore defined by

$${}^{t+\Delta t}_t F_{ij} = \frac{\partial ({}^{t+\Delta t}\mathbf{x}_i)}{\partial {}^t\mathbf{x}_j} = {}^{t+\Delta t}_t x_{i,j} \quad (2.1)$$



Or,

$${}^{t+\Delta t}_t F_{ij} = \frac{\partial ({}^t x_i + {}^t \Delta u_i)}{\partial {}^t x_j} = \delta_{ij} + \frac{\partial {}^t \Delta u_i}{\partial {}^t x_j} \quad (2.2)$$

When  ${}^{t+\Delta t}_t \mathbf{F}$  is non-singular, the polar decomposition theorem [44] allows a decomposition of the form:

$${}^{t+\Delta t}_t F_{ij} = {}^{t+\Delta t}_t R_{ik} {}^{t+\Delta t}_t U_{kj} \quad (2.3)$$

where  ${}^{t+\Delta t}_t \mathbf{R}$  is an orthogonal (rotation) tensor representing the material rotation and  ${}^{t+\Delta t}_t \mathbf{U}$  is a positive definite symmetric tensor called right stretch tensor. The right stretch tensor can be diagonalized by the following transformation to obtain the principal stretches  ${}^{t+\Delta t}_t \lambda_i$ :

$${}^{t+\Delta t}_t U_{ij}^p = {}^{t+\Delta t}_t Q_{ik} {}^{t+\Delta t}_t Q_{jl} {}^{t+\Delta t}_t U_{kl} \quad (2.4)$$

where  ${}^{t+\Delta t}_t [Q]$  is orthogonal (transformation) tensor and

$${}^{t+\Delta t}_t \lambda_i = {}^{t+\Delta t}_t U_{ii}^p (no\ sum) \quad (2.5)$$

The tensor  ${}^{t+\Delta t}_t \mathbf{R}$  and the transformation matrix  ${}^{t+\Delta t}_t [Q]$  are used in the development of an objective stress measure while the incremental logarithmic strain tensor is obtained from the  ${}^{t+\Delta t}_t \lambda_i$ .

## 2.3 Stress Measures

It is essential that an objective stress measure be used in the incremental theory of constitutive modeling to account for the rigid body rotation that may accompany deformation. The Cauchy stress tensor, which has great physical significance, is not objective and hence cannot be used directly in a constitutive equation. There are numerous objective stress measures (See [45], [46]), each with particular advantages and disadvantages. Some of them are discussed below:

One of the commonly used objective stress tensor is the second Piola-Kirchoff stress tensor  ${}^{t+\Delta t}_t \mathbf{S}$  which can be related to the Cauchy stress tensor  ${}^{t+\Delta t}_t \boldsymbol{\sigma}$  using the concept

of equivalent work between two configurations [47]:

$${}^{t+\Delta t}_t S_{ij} = \frac{{}^t \rho}{{}^{t+\Delta t}_t \rho} {}^{t+\Delta t}_t x_{i,m} {}^{t+\Delta t}_t \sigma_{mn} {}^{t+\Delta t}_t x_{j,n}. \quad (2.6)$$

Here,  ${}^t \rho$  and  ${}^{t+\Delta t}_t \rho$  are the densities at time  $t$  and  $t + \Delta t$  respectively and  ${}^{t+\Delta t}_t x_{i,m}$  denotes the derivative of  ${}^t x_i$  with respect to  ${}^{t+\Delta t}_t x_m$ . The second Piola-Kirchoff stress tensor is energy conjugate with the Green-Lagrange strain tensor. This energy conjugate pair is used in the equation for predicting displacements in a predictor corrector solution procedure (see section 3.6.2).

Another commonly used objective stress rate measure is the Jaumann stress rate  $\dot{\bar{\sigma}}$ . It is related to the Cauchy rate  $\dot{\sigma}$  by

$${}^t \dot{\bar{\sigma}}_{ij} \Delta t = {}^t \dot{\sigma}_{ij} \Delta t - {}^t \sigma_{ik} ({}^t W_{jk} \Delta t) - {}^t \sigma_{jk} ({}^t W_{ik} \Delta t) \quad (2.7)$$

where

$${}^t W_{ij} \Delta t = \frac{1}{2} ({}^t \Delta u_{i,j} - {}^t \Delta u_{j,i}) \quad (2.8)$$

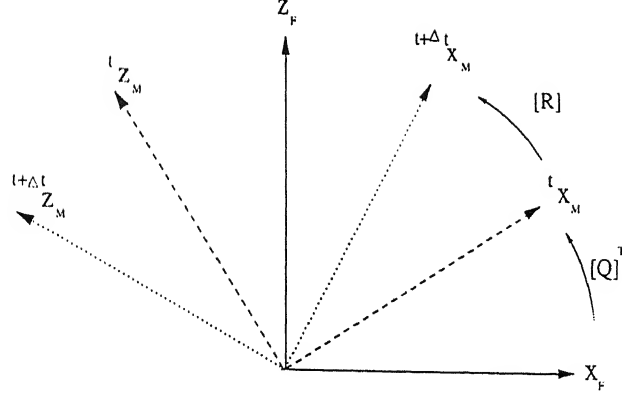
represents the components of the incremental rotation tensor. Here,  ${}^{t+\Delta t}_t \Delta u$  denotes the derivative of the incremental displacement vector  ${}^t \Delta u$  with respect to  ${}^t x$ .

As pointed out by Metzger and Dubey [48], it is important that the stress measure used has to be compatible with the constitutive equation in addition to being objective. An incremental objective stress measure (as against objective stress rate measures) to be used in the generalized Hooke's law as well as in the elasto-plastic constitutive equation is presented below.

Two Cartesian reference frames (see Fig. 2.2) are used for this purpose and they are:

1. The fixed frame.
2. A material frame which rotates and translates along with the material particle.

The material frame is defined so as to coincide with the principal axes of the right stretch tensor at time  $t$  so that the initially orthogonal axes do not get skewed at time  $t + \Delta t$ .



The fixed frame is denoted by subscript F.  
The material frame is denoted by subscript M.

Figure 2.2: Fixed and Material Frames of references.

The first step is the transformation of the components of the Cauchy stress tensor at time  $t$  from the fixed frame to the material frame:

$${}^t\sigma_{ij}^M = {}^{t+\Delta t}_t Q_{ik} {}^{t+\Delta t}_t Q_{jl} {}^t\sigma_{kl}. \quad (2.9)$$

The increment in the components of the Cauchy stress tensor with respect to the material axes,  ${}_t\Delta\sigma_{ij}^M$ , is added to  ${}^t\sigma_{ij}^M$  to obtain the stress components at time  $t+\Delta t$  with respect to the material frame of reference:

$${}^{t+\Delta t}\sigma_{ij}^M = {}^t\sigma_{ij}^M + {}_t\Delta\sigma_{ij}^M. \quad (2.10)$$

The final transformation from the frame at time  $t + \Delta t$  to the fixed frame gives the components of the Cauchy stress tensor at time  $t + \Delta t$ .

$${}^{t+\Delta t}\sigma_{ij} = {}^{t+\Delta t}_t Q_{ki} {}^{t+\Delta t}_t R_{kl} {}^{t+\Delta t}\sigma_{lm}^M {}^{t+\Delta t}_t R_{nm} {}^{t+\Delta t}_t Q_{nj}. \quad (2.11)$$

The equations (2.9), (2.10) and (2.11) can be combined together to give a relation between the components of the Cauchy stress tensor at times  $t$  and  $t+\Delta t$  and the increment in the components with respect to the material frame:

$${}^{t+\Delta t}\sigma_{ij} = {}^{t+\Delta t}_t Q_{ki} {}^{t+\Delta t}_t R_{kl} ({}^{t+\Delta t}_t Q_{lm} {}^t\sigma_{mn} {}^{t+\Delta t}_t Q_{on} + {}_t\Delta\sigma_{lo}^M) {}^{t+\Delta t}_t R_{po} {}^{t+\Delta t}_t Q_{pj}. \quad (2.12)$$

The proposed stress and the logarithmic strain measures satisfy the requirement of objectivity and lead to a physically consistent application of the usual constitutive equation.

## 2.4 Strain Measures

The incremental small strain is given by

$${}_t\Delta\varepsilon_{ij} = \frac{1}{2}({}_t\Delta u_{i,j} + {}_t\Delta u_{j,i}) \quad (2.13)$$

The incremental Green Lagrange strain is a non-linear function of the displacement and is given by:

$${}_t\Delta e_{ij} = \frac{1}{2}({}_t\Delta u_{i,j} + {}_t\Delta u_{j,i} + {}_t\Delta u_{k,i}{}_t\Delta u_{k,j}) \quad (2.14)$$

These two strain measures occur in the virtual work expression at time  $t + \Delta t$  and its transformation to time  $t$  respectively. The components of the Green Lagrange strain tensor are invariant under rigid body rotation of the material, unlike the small strain components. The following are the disadvantages of using one of the above measures in a constitutive law.

1. The solution obtained is dependent upon the size of the increment in the updated Lagrangian formulation unless the increment size is sufficiently small.
2. The components of the strain tensors do not tend to infinite values when the principal stretches tend to zero. Therefore, a constitutive law, which ensures that the appropriate Cauchy stress components tend to negative infinity (as is physically realistic), even though the strain components remain finite, should be used. This difficulty can be avoided by using a strain measure whose components become minus infinity when the principal stretches become zero.

The logarithmic strain measure introduced by Dienes [45] is free from the above disadvantages. The principal incremental logarithmic strain components, which will be used in this work, are defined by

$${}_t\Delta\varepsilon_{ij}^L = \ln({}_t^{t+\Delta t}\lambda_i)\delta_{ij} \quad (2.15)$$

where the  ${}^{t+\Delta t}\lambda_i$  are the principal stretches defined by equation (2.5). The logarithmic strain has the following additional advantage in elasto-plastic analysis. A loading test involving elasto-plastic deformation followed by elastic unloading reveals that the slope of the elastic unloading line is the same as that of the initial elastic line only when the true stress and the logarithmic strain measures are used in a constitutive law [49].

## 2.5 Elastic Constitutive Equation

The elastic constitutive equation used is the generalized Hooke's law relating the increment in stress components with respect to the material frame  $\Delta\sigma_{ij}^M$  and the elastic part  ${}^t\Delta\varepsilon_{ij}^{eL}$  of the principal incremental logarithmic strain components:

$${}^t\Delta\sigma_{ij}^M = C_{ijkl}^E {}^t\Delta\varepsilon_{kl}^{eL}. \quad (2.16)$$

The tensor  $\mathbf{C}^E$  for the isotropic case is given by

$$C_{ijkl}^E = \lambda \delta_{ij} \delta_{kl} + 2\mu \delta_{ik} \delta_{jl} \quad (2.17)$$

where  $\lambda$  and  $\mu$  are Lamé's constants ( $\mu$  is also called as shear modulus). For anisotropic behavior, the tensor  $\mathbf{C}^E$  has to be evaluated with reference to the directions of the principal stretches. The stress and strain measures used in a constitutive equation need not necessarily be energy conjugate with each other. However if it is so, the predicted response in a predictor-corrector scheme will be closer to the actual response.

## 2.6 Elasto-Plastic Constitutive Equation

As stresses developed in a material exceed the yield stress, the elastic constitutive relationship between the stress and strain tensors no longer remains valid. A relationship between the stress and strain based on the von Mises yield criterion and isotropic hardening is presented in this section<sup>1</sup>.

---

<sup>1</sup>In this section the subscript/superscript denoting time have been omitted for sake of convenience.

For an isotropically hardening material, the plastic potential is given by [50]

$$\Psi(\sigma_{ij}, p) = \sigma_{eq}(\sigma_{ij}) - \sigma_y(p). \quad (2.18)$$

Note that

$$\Psi = 0 \quad (2.19)$$

represents the yield criterion. The plastic potential  $\Psi$  depends on the Cauchy stress tensor  $\sigma_{ij}$  through its second invariant  $\sigma_{eq}$  called as equivalent stress and defined by

$$\sigma_{eq} = \left( \frac{3}{2} \sigma'_{ij} \sigma'_{ij} \right)^{\frac{1}{2}} \quad (2.20)$$

where  $\sigma'_{ij}$  is the deviatoric part of  $\sigma_{ij}$ . Further,  $\Psi$  depends on the variable yield stress of the material,  $\sigma_y$ , through a hardening variable  $p$ . For the case of strain hardening,  $p$  is identified as the equivalent plastic strain  $\varepsilon_{eq}^{pL}$ , and is defined as:

$$p \equiv \varepsilon_{eq}^{pL} = \int d\varepsilon_{eq}^{pL} \quad (2.21)$$

where

$$d\varepsilon_{eq}^p = \left( \frac{2}{3} d\varepsilon_{ij}^{pL} d\varepsilon_{ij}^{pL} \right)^{\frac{1}{2}}. \quad (2.22)$$

Here,  $d\varepsilon_{ij}^{pL}$  is the plastic part of the incremental logarithmic strain tensor  $d\varepsilon_{ij}^L$  and the integration in equation (2.21) is to be carried along the particle path. The dependence of  $\sigma_y$  on  $p$  (or  $\varepsilon_{eq}^p$ ) is normally approximated by a power-law type of relationship:

$$\sigma_y \equiv H(\varepsilon_{eq}^p) = (\sigma_y)_o + K(\varepsilon_{eq}^p)^n. \quad (2.23)$$

Here,  $(\sigma_y)_o$  is the yield stress at zero plastic strain,  $K$  is called the hardening coefficient and  $n$  is called as the hardening exponent.

The plastic part of incremental logarithmic strain tensor ( $d\varepsilon_{ij}^{pL}$ ) is obtained from the plastic potential using the following relation:

$$d\varepsilon_{ij}^{pL} = d\lambda \frac{\partial \Psi}{\partial \sigma_{ij}} \quad (2.24)$$

where  $d\lambda$  is a scalar. This equation is called as the flow rule. Differentiation of equation (2.18) with respect to  $\sigma_{ij}$  gives

$$\frac{\partial \Psi}{\partial \sigma_{ij}} = \frac{3}{2\sigma_{eq}} \sigma'_{ij}. \quad (2.25)$$

Using this and the definition of  $d\varepsilon_{eq}^{pL}$  (equation 2.22), one can determine  $d\lambda$  as

$$d\lambda = d\varepsilon_{eq}^p \quad (2.26)$$

Further, the hardening relationship and the yield condition can be used to express  $d\lambda$  as:

$$d\lambda = \frac{d\sigma_y}{H'} = \frac{d\sigma_{eq}}{H'} \quad (2.27)$$

where

$$H' = \frac{d\sigma_y}{d\varepsilon_{eq}^p} = Kn(\varepsilon_{eq}^p)^{n-1} \quad (2.28)$$

is the slope of the hardening curve. Substitution of equations (2.25) and (2.27) in equation (2.24) leads to the following constitutive equation:

$$d\varepsilon_{ij}^{pL} = \frac{3d\sigma_{eq}}{2H'\sigma_{eq}} \sigma'_{ij} \quad (2.29)$$

This constitutive relationship between the deviatoric stress tensor and the plastic part of incremental logarithmic strain tensor is not really convenient for the updated Lagrangian formulation for which the incremental stress-strain relationship is needed. This can be obtained from equation (2.29) as follows:

$$d\varepsilon_{ij}^{pL} = \frac{3\sigma'_{ij}}{2H'\sigma_{eq}} \frac{\partial \sigma_{eq}}{\partial \sigma_{kl}} d\sigma_{kl}. \quad (2.30)$$

Note that, from equations (2.18) and (2.25), one can get

$$\frac{\partial \sigma_{eq}}{\partial \sigma_{kl}} = \frac{\partial \Psi}{\partial \sigma_{kl}} = \frac{3}{2\sigma_{eq}} \sigma'_{kl}. \quad (2.31)$$

Substitution of equation (2.31) in equation (2.30) leads to the following incremental

plastic stress strain relationship:

$$d\varepsilon_{ij}^p = \frac{9\sigma'_{ij}\sigma'_{kl}}{4H'\sigma_{eq}^2} d\sigma_{kl}. \quad (2.32)$$

The incremental elastic stress strain relationship (equations (2.16) - (2.17)) can now be written as:

$$d\varepsilon_{ij}^{eL} = \frac{1}{E}[-\nu d\sigma_{kk}\delta_{ij} + (1 + \nu)d\sigma_{ij}] \quad (2.33)$$

where  $d\varepsilon_{ij}^{eL}$  is the elastic part of  $d\varepsilon_{ij}^L$ ,  $E$  is the Young's modulus and  $\nu$  is the Poisson's ratio. Adding the two relationship equations, one can get

$$\begin{aligned} d\varepsilon_{ij}^L &= d\varepsilon_{ij}^{eL} + d\varepsilon_{ij}^p \\ &= \left[ \frac{-\nu}{E} \delta_{ij} \delta_{kl} + \frac{1 + \nu}{E} \delta_{ik} \delta_{jl} + \frac{9\sigma'_{ij}\sigma'_{kl}}{4H'\sigma_{eq}^2} \right] d\sigma_{kl}. \end{aligned} \quad (2.34)$$

This is the incremental elasto-plastic stress strain relationship needed in the updated Lagrangian formulation. However, it is the following inverse relationship that is more useful:

$$d\sigma_{ij} = C_{ijkl}^{EP} d\varepsilon_{kl}^L \quad (2.35)$$

where

$$C_{ijkl}^{EP} = 2\mu \left( \delta_{ik} \delta_{jl} + \frac{\nu}{1 - 2\nu} \delta_{ij} \delta_{kl} - \frac{9\mu\sigma'_{ij}\sigma'_{kl}}{2(3\mu + H')\sigma_{eq}^2} \right). \quad (2.36)$$

Note that the stress increment appearing in equation (2.35) must be an objective stress increment in the sense that  $d\sigma_{ij}$  must reduce to a zero tensor in the event of the increment being a pure rigid rotation. The incremental objective stress measure to be used in the present work has been described in section 2.3.

The relationship (2.35) has been derived assuming the increment size to be small. When a large size increment is to be used, the relationship (2.35) takes the following form with respect to the material frame.



$${}^t\Delta\sigma_{ij}^M = \int_t^{t+\Delta t} {}^tC_{ijkl}^{EP} d({}^t\Delta\varepsilon_{kl}^L) \quad (2.37)$$

where

$${}^tC_{ijkl}^{EP} = 2\mu \left( \delta_{ik}\delta_{jl} + \frac{\nu}{1-2\nu}\delta_{ij}\delta_{kl} - \frac{9\mu {}^t\sigma'_{ij} {}^t\sigma'_{ij}}{2(3\mu + Kn({}^t\varepsilon_{eq}^p)^{n-1}) {}^t\sigma_{eq}^2} \right). \quad (2.38)$$

Here,  $H'$  has been replaced by the expression (2.28) and the left superscript  $t$  has been added to make it explicit that these quantities are to be evaluated at that time.

## 2.7 Incremental Updated Lagrangian Formulation

The objective of the updated Lagrangian formulation is to establish static equilibrium in the configuration at time  $t+\Delta t$  when all static variables at time  $t$  are known. The principle of virtual work requires that

$$\int_{t+\Delta t V} {}^{t+\Delta t}\sigma_{ij} \delta \left( {}^{t+\Delta t}\varepsilon_{ij} \right) d{}^{t+\Delta t}V = {}^{t+\Delta t}R \quad (2.39)$$

where

${}^{t+\Delta t}\sigma_{ij}$  = Cauchy stress tensor at time  $t+\Delta t$ ,

${}^{t+\Delta t}V$  = volume at time  $t+\Delta t$ .

The quantity  $\delta {}^{t+\Delta t}\varepsilon_{ij}$  is the virtual linear strain tensor and is defined as

$$\delta {}^{t+\Delta t}\varepsilon_{ij} = \frac{1}{2} \left( \frac{\partial \delta_t \Delta u_i}{\partial {}^{t+\Delta t}x_j} + \frac{\partial \delta_t \Delta u_j}{\partial {}^{t+\Delta t}x_i} \right) \quad (2.40)$$

where

$\delta_t \Delta u_i$  = virtual incremental displacement vector at time  $t$ ,  ${}^{t+\Delta t}x_i$  = position vector at time  $t + \Delta t$ .

Further,  ${}^{t+\Delta t}R$  is the virtual work of the external forces and is given by

$${}^{t+\Delta t}R = \int_{{}_t^{t+\Delta t}S_t} {}^{t+\Delta t}t_i \delta_t \Delta u_i d{}^{t+\Delta t}S \quad (2.41)$$

where the traction vector  ${}^{t+\Delta t}t_i$ , specified on the boundary  ${}^{t+\Delta t}S_t$ , is given by

$${}^{t+\Delta t}t_i = {}^{t+\Delta t}\sigma_{ij} {}^{t+\Delta t}n_j. \quad (2.42)$$

Here,  ${}^{t+\Delta t}n_j$  is the unit outward normal vector to  ${}^{t+\Delta t}S_t$ .

The main difficulty in the application of equation (2.39) is that the configuration at time  $t+\Delta t$  is unknown. The virtual work expression at time  $t+\Delta t$  is transformed to an integral over the volume at time  $t$  [51]. It is assumed that the external load term (2.41) is deformation independent for the formulation of the governing equation. The expression (2.39) after the transformation becomes

$$\int_{{}_tV} {}^{t+\Delta t}S_{ij} \delta({}_t^{t+\Delta t}e_{ij}) d{}^tV = {}^{t+\Delta t}R \quad (2.43)$$

Where, the virtual Green-Lagrange strain tensor  $\delta({}_t^{t+\Delta t}e_{ij})$  is defined by

$$\delta({}_t^{t+\Delta t}e_{ij}) = \delta \frac{1}{2} [{}_t\Delta u_{i,j} + {}_t\Delta u_{j,i} + {}_t\Delta u_{k,i} {}_t\Delta u_{k,j}] \quad (2.44)$$

The second Piola-Kirchoff stress tensor can be decomposed as

$${}^{t+\Delta t}S_{ij} = {}_tS_{ij} + {}_t\Delta S_{ij} = {}_t\sigma_{ij} + {}_t\Delta S_{ij}. \quad (2.45)$$

Further, the virtual Green-Lagrange strain tensor can be decomposed as

$$\delta({}_t^{t+\Delta t}e_{ij}) = \delta({}_t\Delta e_{ij}) = \delta({}_t\Delta \varepsilon_{ij} + {}_t\Delta \eta_{ij}) \quad (2.46)$$

where

$${}_t\Delta \varepsilon_{ij} = \frac{1}{2}({}_t\Delta u_{i,j} + {}_t\Delta u_{j,i}), \quad (2.47)$$

$${}_t\Delta \eta_{ij} = \frac{1}{2}({}_t\Delta u_{k,i} {}_t\Delta u_{k,j}). \quad (2.48)$$

Therefore, equation (2.43) can be written with incremental decomposition as

$$\int_{tV} \Delta S_{ij} \delta({}_t\Delta \varepsilon_{ij}) d^tV + \int_{tV} \Delta S_{ij} \delta({}_t\Delta \eta_{ij}) d^tV +$$

$$\int_{tV} {}^t\sigma_{ij} \delta({}_t\Delta \eta_{ij}) d^tV + \int_{tV} {}^t\sigma_{ij} \delta({}_t\Delta \varepsilon_{ij}) d^tV = {}^{t+\Delta t}R. \quad (2.49)$$

The above equation is simplified by neglecting the second integral, which is a higher order term, and approximating  ${}_t\Delta S_{ij}$  as  ${}^tC_{ijkl}^{EP} {}^t\Delta \varepsilon_{kl}$ :

$$\begin{aligned} & \int_{tV} {}^tC_{ijkl}^{EP} {}^t\Delta \varepsilon_{kl} \delta({}_t\Delta \varepsilon_{ij}) d^tV + \int_{tV} {}^t\sigma_{ij} \delta({}_t\Delta \eta_{ij}) d^tV \\ & + \int_{tV} {}^t\sigma_{ij} \delta({}_t\Delta \varepsilon_{ij}) d^tV = {}^{t+\Delta t}R. \end{aligned} \quad (2.50)$$

The linearized equation, when solved, will yield only approximate displacement, strain and stress fields. The approximate quantities are denoted by a right superscript (1). The error due to the approximation involved is calculated from equation (2.39) as

$$Error = {}^{t+\Delta t}R - \int_{t+\Delta tV^{(1)}} {}^{t+\Delta t}\sigma_{ij}^{(1)} \delta({}_t^{t+\Delta t}\varepsilon_{ij}^{(1)}) d^{t+\Delta t}V^{(1)}. \quad (2.51)$$

This error is generally minimized by an iterative predictor-corrector scheme described in section 3.6.2.

## 2.8 Boundary Conditions for 3-D Deep Drawing of Rectangular Sheet

The sheet or the domain is as shown in figure 2.3.

The global coordinate system is also shown. Since the problem has two axes of symmetry, only one fourth of the sheet(domain) is considered for analysis as shown in figure 2.4.

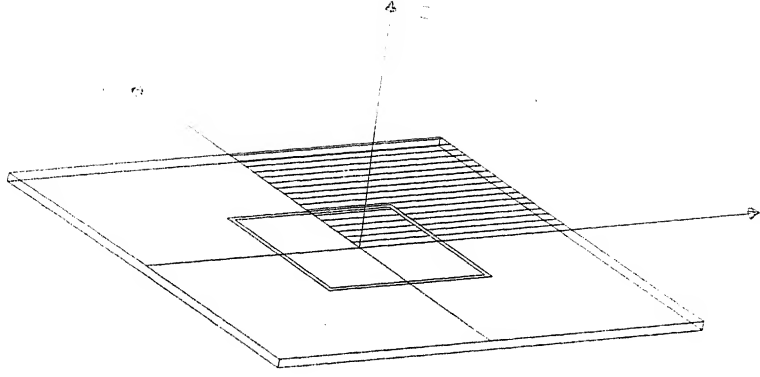


Figure 2.3: The complete domain of the Problem.

## 2.8.1 Initial Boundary Conditions

The boundary conditions (both essential and natural) during the starting of the analysis are discussed below.

### 2.8.1.1 The Sheet-Punch Interface

The sheet-punch interface is represented by face  $OABC$  in figure 2.4. The sticking friction condition is assumed at the interface. However, a node at the interface may loose contact depending upon direction of the vertical reaction force. For the nodes in contact,  $z$ -component of incremental displacement vector is specified at the interface. For the nodes not in contact, the incremental traction vector is zero. Thus,

1.  ${}^{t+\Delta t}F_z < 0$ (contact nodes),    *Essential boundary condition:*

$${}_t\Delta u_x = 0, \quad {}_t\Delta u_y = 0, \quad {}_t\Delta u_z = \text{specified.} \quad (2.52)$$

2.  ${}^{t+\Delta t}F_z > 0$  (non contact nodes),    *Natural boundary condition:*

$${}_t\Delta t_x = 0, \quad {}_t\Delta t_y = 0, \quad {}_t\Delta t_z = 0. \quad (2.53)$$

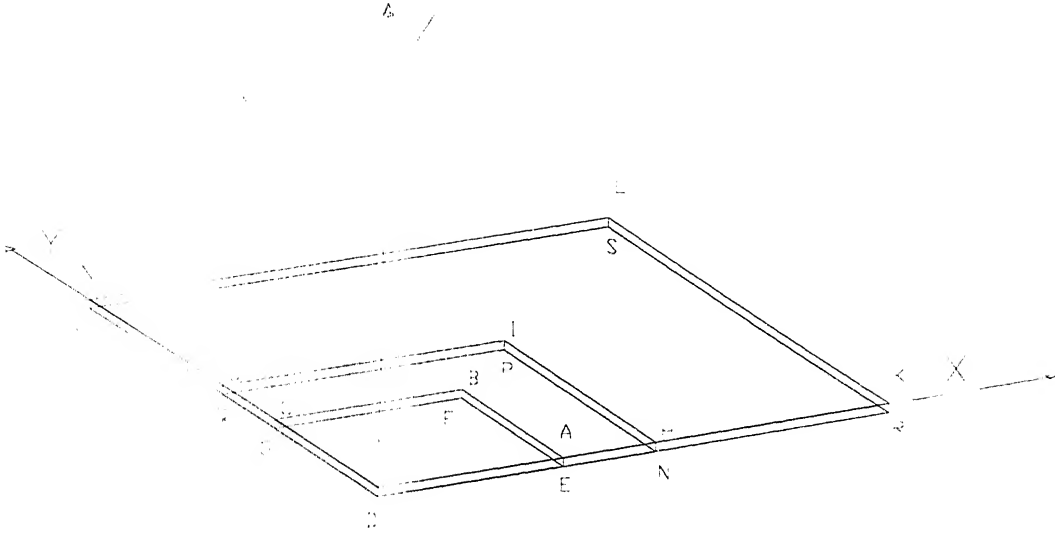


Figure 2.4: The domain considered for analysis.

#### 2.8.1.2 The Free Surfaces

The free surfaces, i.e. region where applied traction is zero, are represented by planes  $ABCJIHA, RKL SR, TSLMT, NEDGQPN$  in figure 2.4. Therefore, the boundary conditions on these planes are:

*Natural boundary condition:*

$${}_t\Delta t_x = 0, \quad {}_t\Delta t_y = 0, \quad {}_t\Delta t_z = 0. \quad (2.54)$$

#### 2.8.1.3 X-Z Plane of Symmetry

Because of symmetry, normal component of incremental displacement vector and shear component of incremental traction vector are zero on this boundary. This surface is represented by plane  $RNEDOAHKR$  in figure 2.4. Thus,

*Natural boundary condition:*

$${}_t\Delta t_x = 0, \quad {}_t\Delta t_z = 0,$$

*Essential boundary condition:*

$${}_t\Delta u_y = 0. \quad (2.55)$$

#### 2.8.1.4 Y-Z Plane of Symmetry

Because of symmetry, normal component of incremental displacement vector and shear component of incremental traction vector are zero on this boundary. This surface is represented by plane *TMJCODGQT* in figure 2.4. Thus, *Natural boundary condition:*

$${}_t\Delta t_y = 0 \quad , \quad {}_t\Delta t_z = 0,$$

*Essential boundary condition:*

$${}_t\Delta u_x = 0. \quad (2.56)$$

#### 2.8.1.5 Sheet-Die Interface

Let  $f$  be the coefficient of friction between the sheet-die interface. Then the boundary conditions in x and y directions are:

1. No slip:

$${}_t\Delta u_x = 0, \quad {}_t\Delta u_y = 0 \quad : \text{if } \sqrt{{}_t t_x^2 + {}_t t_y^2} < f |{}_t t_z| \quad (2.57)$$

2. Slip:

$${}_t\Delta t_x = -f_t \Delta t_x \cos \theta, \quad {}_t\Delta t_y = -f_t \Delta t_x \sin \theta \quad : \text{if } \sqrt{{}_t t_x^2 + {}_t t_y^2} \geq f |{}_t t_z| \quad (2.58)$$

where  $\theta$  is the angle made by the slip direction with positive x-axis. The boundary condition in z-direction is given by: *Essential boundary condition:*

$${}_t\Delta u_z = 0. \quad (2.59)$$

### 2.8.1.6 Surface with Blank-Holding Force

The Blank Holder force is applied on the top portion of the plate represented by the planes *HIJMLKH* in figure 2.4. It is assumed that this force is uniformly distributed and it is applied incrementally. Therefore, this boundary condition is

*Natural boundary condition:*

$${}_t\Delta t_x = 0, \quad {}_t\Delta t_y = 0, \quad {}_t\Delta t_z = \text{specified} \quad (2.60)$$

## 2.8.2 Incremental Boundary Conditions

As the deformation progresses in the sheet(domain), the position of the nodes and related boundary conditions get affected and therefore an incremental updation of boundary condition of nodes in accordance with its position and behavior needs to be done. The following section explains how this is achieved.

### 2.8.2.1 Recognition of State of Nodes

The whole domain is first divided into regions having similar boundary conditions such as those shown in figure 2.5. The nodes are then given different status according to their position and region.

The nodes if, at any particular increment, come under the punch radius or die radius region are checked for penetration and are given specified displacement to project them onto the punch/die profile

### 2.8.2.2 Punch Penetration and Specified Displacement

Suppose a node  $P$ , at some increment, penetrates to the position  $P_1$  or  $P_2$  (in the corner region). The actual location of the point  $P_1$  and  $P_2$  are shown in the sectional views A-A and B-B. The punch profiles and the position vector ( $\underline{t}$ ) of the points  $P_1$  and  $P_2$  with respect to the center of curvature are shown in these sectional views. To avoid the penetration, the actual location of the node should be at  $P_1^*$  (or  $P_2^*$ ) which is obtained

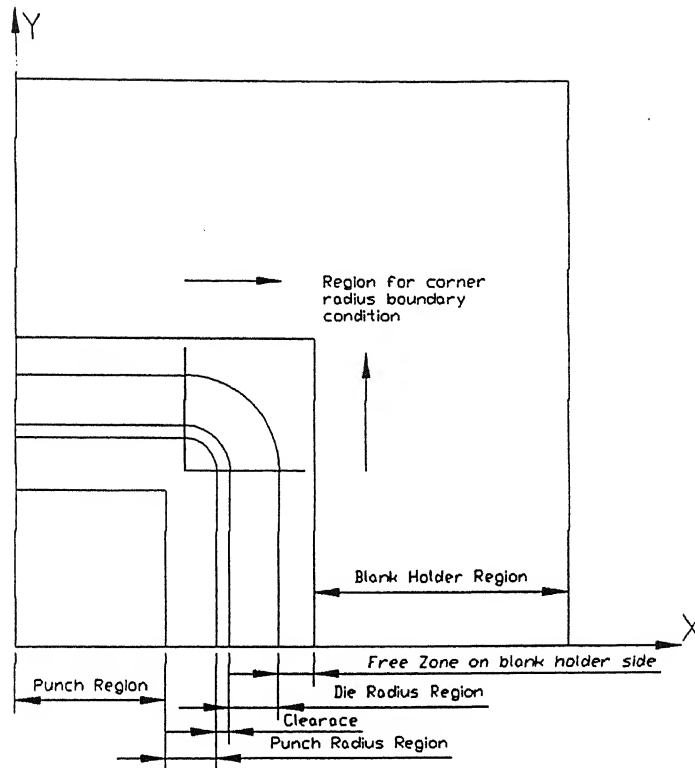


Figure 2.5: Subdivision of domain.

by extending  $\underline{L}$  to the profile. Thus, the boundary condition is applied in the following manner:

- First, the penetration is checked by comparing the magnitude of position vector  $|\underline{L}|$  with the profile radius. Note that the profile radius is bigger than the punch radius in the corner region.
- The required specified displacement is then calculated. It is the difference of the position vector of point  $P$  (position of the node in the previous increment, not shown in figure) and  $P_1$  (or  $P_2$ )
- The whole increment is the repeated so as to get the node on the punch profile.

### 2.8.2.3 Die Penetration and Specified Displacement



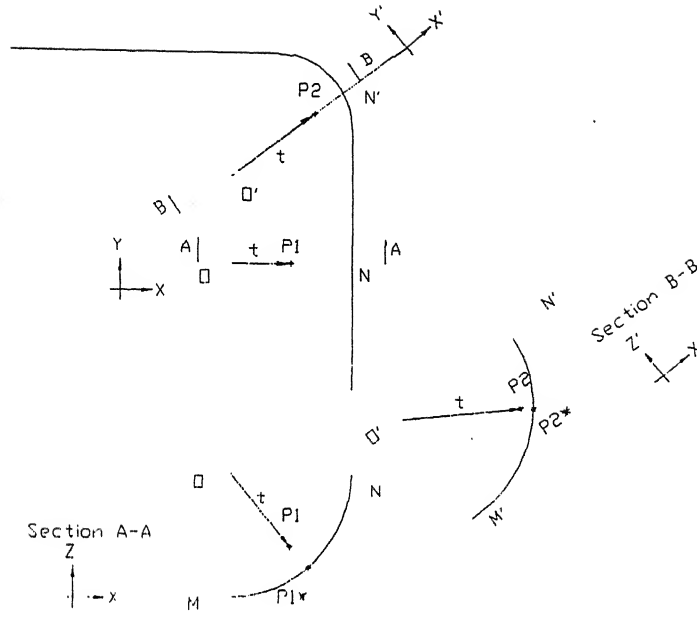


Figure 2.6: Penetration of node in the punch region.

The penetration of a node in the die region is also checked using a criterion similar to that of section 2.8.2.2. Suppose a node  $P$  penetrates into the die profile to a point  $P_1$  or  $P_2$  (in the corner region) at some increment. The corresponding projection on the die profile along the vector  $\underline{t}$  is shown by positions  $P_1^*$  or  $P_2^*$ .

All the nodes lying in the region of die radius are first checked for penetration and then the required specified displacement is calculated. The required specified displacement is equal to the difference of position vectors of points  $P$  and that of point  $P_1^*$  or  $P_2^*$ . The whole increment is then repeated so as to get the node on the die profile.

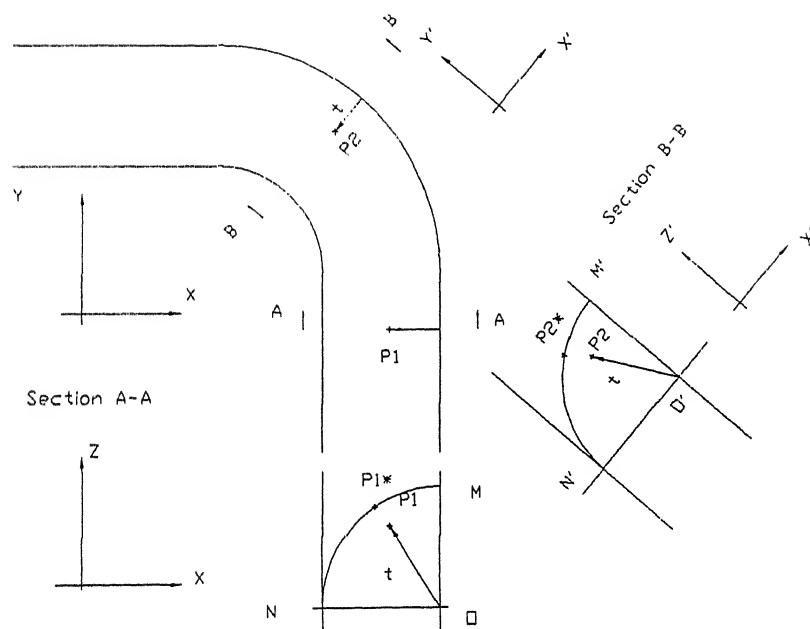


Figure 2.7: Penetration of node in the die region.

# Chapter 3

## Finite Element Formulation

In this chapter the finite element formulation of the problem is developed. First the matrix notation used in the development is discussed in section 3.1. Then the finite element equations are derived in section 3.2. The static condensation and other numerical aspects of the solution procedure are explained in the remaining sections.

### 3.1 Matrix Notation

For the 3-D case, the components of the tensors,  ${}_t\Delta\epsilon$ ,  ${}_t\Delta\eta$  and  ${}_t\Delta\epsilon^L$  are represented in array form as follows:

$${}_t\{\Delta\epsilon\}^T = \{{}_t\Delta\epsilon_{xx}, {}_t\Delta\epsilon_{yy}, {}_t\Delta\epsilon_{zz}, 2{}_t\Delta\epsilon_{xy}, 2{}_t\Delta\epsilon_{yz}, 2{}_t\Delta\epsilon_{xz}\}, \quad (3.1)$$

$${}_t\{\Delta\eta\}^T = \{{}_t\Delta u_{,x}, {}_t\Delta u_{,y}, {}_t\Delta u_{,z}, {}_t\Delta v_{,x}, {}_t\Delta v_{,y}, \dots\}, \quad (3.2)$$

$${}_t\{\Delta\epsilon^L\}^T = \{{}_t\Delta\epsilon_{xx}^L, {}_t\Delta\epsilon_{yy}^L, {}_t\Delta\epsilon_{zz}^L, {}_t\Delta\epsilon_{xy}^L, {}_t\Delta\epsilon_{yz}^L, {}_t\Delta\epsilon_{xz}^L\}. \quad (3.3)$$

The components of all stress tensors are written as arrays with respective components placed in the following manner:

$$\{\sigma\}^T = \{\sigma_{xx}, \sigma_{yy}, \sigma_{zz}, \sigma_{xy}, \sigma_{yz}, \sigma_{xz}\}. \quad (3.4)$$

Two matrix forms of the tensor  ${}^lC_{ijkl}^{EP}$  ( given by equation 2.38) are needed:

1.  ${}^t[C^{EP}]$  for the constitutive relationship :  ${}^t\{\Delta S\} = {}^t[C^{EP}]' {}^t\{\Delta \varepsilon\}$ ,
2.  ${}^t[C^{EP}]'$  for the constitutive relationship :  ${}^t\{\Delta \sigma^M\} = {}^t[C^{EP}] {}^t\{\Delta \varepsilon\}^L$ .

For isotropic case they are given by:

$${}^t[C^{EP}] = \left( [C^E] - \frac{[C^E] {}^t\{a\} {}^t\{a\}^T [C^E]}{{}^tH + {}^t\{a\}^T [C^E] {}^t\{a\}} \right), \quad (3.5)$$

$${}^t[C^{EP}]' = \left( [C^E]' - \frac{[C^E]' {}^t\{a\} {}^t\{a\}^T [C^E]'}{{}^tH + {}^t\{a\}^T [C^E]' {}^t\{a\}} \right). \quad (3.6)$$

In the above equations,

$${}^t\{a\}^T = \frac{3}{2 {}^t\sigma_{eq}} \{ {}^t\sigma'_{xx} \quad {}^t\sigma'_{yy} \quad {}^t\sigma'_{zz} \quad {}^t2\sigma'_{xy} \quad {}^t2\sigma'_{yz} \quad {}^t2\sigma'_{zx} \} \quad (3.7)$$

and  $\sigma'_{ij}$  represents the components of the deviatoric part of the Cauchy stress at time  $t$ . For an isotropic material,  $[C^E]$  and  $[C^E]'$  for the 3-D case are given by

$$[C^E] = \frac{E}{(1+\nu)(1-2\nu)} \begin{bmatrix} 1-\nu & \nu & \nu & 0 & 0 & 0 \\ \nu & 1-\nu & \nu & 0 & 0 & 0 \\ \nu & \nu & 1-\nu & 0 & 0 & 0 \\ 0 & 0 & 0 & \frac{1-2\nu}{2} & 0 & 0 \\ 0 & 0 & 0 & 0 & \frac{1-2\nu}{2} & 0 \\ 0 & 0 & 0 & 0 & 0 & \frac{1-2\nu}{2} \end{bmatrix}, \quad (3.8)$$

$$[C^E]' = \frac{E}{(1+\nu)(1-2\nu)} \begin{bmatrix} 1-\nu & \nu & \nu & 0 & 0 & 0 \\ \nu & 1-\nu & \nu & 0 & 0 & 0 \\ \nu & \nu & 1-\nu & 0 & 0 & 0 \\ 0 & 0 & 0 & 1-2\nu & 0 & 0 \\ 0 & 0 & 0 & 0 & 1-2\nu & 0 \\ 0 & 0 & 0 & 0 & 0 & 1-2\nu \end{bmatrix}. \quad (3.9)$$

Equation (2.50) can be written in the following form owing to the symmetries in  ${}^t\mathbf{C}^{EP}$ ,  ${}^t\Delta\epsilon$ ,  ${}^t\Delta\eta$ , and  ${}^t\sigma$ :

$$\int_{t_V} \delta({}^t\{\Delta\epsilon\}^T) {}^t[C^{EP}]_t \{\Delta\epsilon\} d^tV + \int_{t_V} \delta({}^t\{\Delta\eta\}^T) {}^t[T]_t \{\Delta\eta\} d^tV + \int_{t_V} \delta({}^t\{\Delta\epsilon\}^T) {}^t\{\sigma\} d^tV = {}^{t+\Delta t} R. \quad (3.10)$$

Here, the matrix  ${}^t[T]$  is given by

$${}^t[T] = \begin{bmatrix} {}^t[\Sigma] & 0 & 0 \\ 0 & {}^t[\Sigma] & 0 \\ 0 & 0 & {}^t[\Sigma] \end{bmatrix} \quad (3.11)$$

where

$${}^t[\Sigma] = \begin{bmatrix} {}^t\sigma_{xx} & {}^t\sigma_{xy} & {}^t\sigma_{xz} \\ {}^t\sigma_{xy} & {}^t\sigma_{yy} & {}^t\sigma_{yz} \\ {}^t\sigma_{xz} & {}^t\sigma_{yz} & {}^t\sigma_{zz} \end{bmatrix}. \quad (3.12)$$

## 3.2 Finite Element Equations

The domain is discretized into a number of elements and the incremental displacement field is approximated over each element by

$${}^t\{\Delta u\} = \begin{Bmatrix} {}^t\Delta u_x \\ {}^t\Delta u_y \\ {}^t\Delta u_z \end{Bmatrix} = {}^t[\Phi]_t \{\Delta u\}^e \quad (3.13)$$

where the elemental incremental displacement vector  ${}^t\{\Delta u\}^e$  for an  $n$ -noded element is given by

$${}^t\{\Delta u\}^{eT} = \{ {}^t\Delta u_x^1, {}^t\Delta u_y^1, {}^t\Delta u_z^1, \dots, {}^t\Delta u_x^n, {}^t\Delta u_y^n, {}^t\Delta u_z^n \}. \quad (3.14)$$

The quantities  ${}^t\Delta u_x^i$ ,  ${}^t\Delta u_y^i$ ,  ${}^t\Delta u_z^i$  stand for the unknown incremental displacements of node  $i$  in  $x, y$  and  $z$  directions respectively and the matrix  ${}^t[\Phi]$  is defined by

$${}^t[\Phi] = \begin{bmatrix} {}^t\{\Phi_1\}^T \\ {}^t\{\Phi_2\}^T \\ {}^t\{\Phi_3\}^T \end{bmatrix} \quad (3.15)$$

where

$${}^t\{\Phi_1\}^T = \{ {}^tN_1, 0, 0, {}^tN_2, 0, 0, {}^tN_3, \dots \},$$

$${}^t\{\Phi_2\}^T = \{ 0, {}^tN_1, 0, 0, {}^tN_2, 0, 0, \dots \},$$

$${}^t\{\Phi_3\}^T = \{ 0, 0, {}^tN_1, 0, 0, {}^tN_2, 0, \dots \}. \quad (3.16)$$

The  ${}^tN_i$ , which are functions of  $({}^tx, {}^ty, {}^tz)$  are called as shape functions. The number of nodes and the corresponding shape functions are chosen on the basis of convergence criteria. For the problem under consideration, 8-noded brick element with tri-linear shape functions [53] is used.

The strain field is expressed in terms of the nodal displacements by differentiating (3.13) and using the expressions (2.47 and 2.48). This leads to

$${}^t\{\Delta\varepsilon\} = {}^t[B_L]{}^t\{\Delta u\}^e, \quad (3.17)$$

$${}^t\{\Delta\eta\} = {}^t[B_N]{}^t\{\Delta u\}^e \quad (3.18)$$

where

$${}^t[B_L] = \begin{bmatrix} {}^t\{\Phi_1\}_{,x}^T \\ {}^t\{\Phi_2\}_{,y}^T \\ {}^t\{\Phi_3\}_{,z}^T \\ {}^t\{\Phi_2\}_{,x}^T + {}^t\{\Phi_1\}_{,y}^T \\ {}^t\{\Phi_3\}_{,y}^T + {}^t\{\Phi_2\}_{,z}^T \\ {}^t\{\Phi_1\}_{,z}^T + {}^t\{\Phi_3\}_{,x}^T \end{bmatrix} \quad (3.19)$$

$${}^t[B_N]^T = \left[ {}^t\{\Phi_1\}_{,x}, {}^t\{\Phi_1\}_{,y}, {}^t\{\Phi_1\}_{,z}, {}^t\{\Phi_2\}_{,x}, {}^t\{\Phi_2\}_{,y}, \dots \right]. \quad (3.20)$$

Using equations (3.13), (3.17) and (3.18), the contribution to the integral (3.10) over a typical element  $e$  with volume  $V^e$  is

$$\delta \left( {}^t\{\Delta u\}^{eT} \right) \left( \int_{V^e} {}^t[B_L]^T {}^t[C^{EP}] {}^t[B_L] dV^e \right) {}^t\{\Delta u\}^e +$$

$$\delta \left( {}^t\{\Delta u\}^{eT} \right) \left( \int_{V^e} {}^t[B_N]^T {}^t[T] {}^t[B_N] dV^e \right) {}^t\{\Delta u\}^e +$$

$$\delta \left( {}^t\{\Delta u\}^{eT} \right) \left( \int_{V^e} {}^t[B_L]^T {}^t[\sigma] dV^e \right) = \delta \left( {}^t\{\Delta u\}^{eT} \right) {}^{t+\Delta t}\{F\}^e. \quad (3.21)$$

The contribution to the term  ${}^{t+\Delta t}R$  is expressed in terms of the elemental external force vector  ${}^{t+\Delta t}\{F\}^e$  using a standard procedure [53]. Since the variation in the displacement vector is arbitrary, the above equation can be written as

$${}^t[K]^e {}^t\{\Delta u\}^e + {}^t\{f\}^e = {}^{t+\Delta t}\{F\}^e \quad (3.22)$$

where the elemental stiffness matrix  ${}^t[K]^e$  is given by

$${}^t[K]^e = {}^t[K_L]^e + {}^t[K_{NL}]^e, \quad (3.23)$$

$${}^t[K_L]^e = \int_{V^e} {}^t[B_L]^T {}^t[C^{EP}] {}^t[B_L] dV^e, \quad (3.24)$$

$${}^t[K_{NL}]^e = \int_{V^e} {}^t[B_N]^T {}^t[T] {}^t[B_N] dV^e \quad (3.25)$$

and the elemental internal force vector is

$${}^t\{f\}^e = \int_{V^e} {}^t[B_L]^T {}^t[\sigma] dV^e. \quad (3.26)$$

The elemental stiffness matrix  ${}^t[K]^e$  along with the elemental force vectors  ${}^t\{f\}^e$  and  ${}^{t+\Delta t}\{F\}^e$  are assembled to obtain the global equation:

$${}^t[K]_t \{\Delta u\} + {}^t\{f\} = {}^{t+\Delta t}\{F\}. \quad (3.27)$$

Here,  ${}^t[K]$  is the global stiffness matrix,  ${}^t\{f\}$  is the global internal force vector at time  $t$  and  ${}^{t+\Delta t}\{F\}$  is the global external force vector at time  $t + \Delta t$ . Decomposing  ${}^{t+\Delta t}\{F\}$ , equation (3.27) can be written as

$${}^t[K]_t \{\Delta u\} + {}^t\{f\} = {}^t\{F\} + {}_t\{\Delta F\}. \quad (3.28)$$

Here,  ${}^t\{F\}$  is the global external force vector at time  $t$  and  ${}_t\{\Delta F\}$  is the global incremental force vector from time  $t$  to  $t + \Delta t$ . In updated Lagrangian formulation, it is assumed that the equilibrium equations are satisfied exactly at time  $t$ . Thus

$${}^t\{f\} = {}^t\{F\}. \quad (3.29)$$

Then, equation (3.28) reduces to

$${}^t[K]_t \{\Delta u\} = {}_t\{\Delta F\}. \quad (3.30)$$

This equation is solved to obtain the incremental displacement vector  ${}_t\{\Delta u\}$ . Static condensation of the coefficient matrix and right side vector is carried out before solving



this equation. The condensation procedure is explained in the next section.

### 3.3 Static Condensation Scheme

Since the contact conditions need to be applied in an iterative manner, solving the full storage equations in all the iterations takes an enormously large amount of time, especially when the number of degrees of freedom is high. To reduce the solution time, it is desirable to condense the coefficient matrix and the right side vector to the size involving only those degrees of freedom to which the contact boundary conditions are to be applied. This condensation procedure is described in the next paragraph.

First, the total nodes are divided into two categories. The nodes at which contact conditions are to be applied are called the nodes of type 1. The rest of the nodes are called as nodes of type 2. To facilitate the condensation, the nodes are numbered in such a manner that the nodes of type 1 are numbered first and then the nodes of type 2 are numbered. Then the essential boundary conditions (i.e, the boundary conditions on the incremental displacement vector, which is the primary variable in this case) for the nodes of type 2 are applied to equation (3.30). The essential boundary conditions of the deep drawing process are described in section 2.9.

Next, these equations are partitioned as follows<sup>1</sup>:

$$\begin{bmatrix} [K_{11}] & [K_{12}] \\ [K_{21}] & [K_{22}] \end{bmatrix} \begin{Bmatrix} \{\Delta u_1\} \\ \{\Delta u_2\} \end{Bmatrix} = \begin{Bmatrix} \{\Delta F_1\} \\ \{\Delta F_2\} \end{Bmatrix} \quad (3.31)$$

where  $\{\Delta u_1\}$  denotes the incremental displacement vector corresponding to the nodes of type 1 and  $\{\Delta u_2\}$  contains the incremental displacements of the nodes of type 2. Equation (3.31) can be separated as follows:

$$[K_{11}]\{\Delta u_1\} + [K_{12}]\{\Delta u_2\} = \{\Delta F_1\}, \quad (3.32)$$

$$[K_{21}]\{\Delta u_1\} + [K_{22}]\{\Delta u_2\} = \{\Delta F_2\}. \quad (3.33)$$

---

<sup>1</sup>In this section, the subscript/superscript denoting time have been omitted for the sake of convenience

Solving for  $\{\Delta u_2\}$  from equation (3.33), we get

$$\{\Delta u_2\} = [K_{22}]^{-1}(\{\Delta F_2\} - [K_{21}]\{\Delta u_1\}) \quad (3.34)$$

Substitution of this expression for  $\{\Delta u_2\}$  in equation (3.32) and rearrangement of the resulting equation leads to the following condensed set of approximate equilibrium equations:

$$[\widehat{K}]\{\Delta \widehat{u}\} = \{\Delta \widehat{F}\} \quad (3.35)$$

where

$$[\widehat{K}] = [K_{11}] - [K_{12}][A], \quad (3.36)$$

$$\{\Delta \widehat{u}\} = \{\Delta u_1\}, \quad (3.37)$$

$$\{\Delta \widehat{F}\} = \{\Delta F_1\} - [K_{12}][B], \quad (3.38)$$

$$[A] = [K_{22}]^{-1}[K_{21}], \quad (3.39)$$

$$\{B\} = [K_{22}]^{-1}\{\Delta F_2\}. \quad (3.40)$$

The number of equations in the condensed set (3.35) is equal to the number of degrees of freedom of type 1. The coefficient matrix  $[\widehat{K}]$  and the right side vector  $\{\widehat{F}\}$  are evaluated from equations (3.36-3.40) using the partitioned matrices and vectors of equation (3.31). Note that while evaluating  $[A]$  and  $\{B\}$ , it is not necessary to invert the matrix  $[K_{22}]$ . Instead, one can solve the following equations by the Gauss elimination method:

$$[K_{22}][A] = [K_{21}], \quad (3.41)$$

$$[K_{22}]\{B\} = \{\Delta F_2\}. \quad (3.42)$$

To reduce the computational time further, one can store the upper triangular form of  $[K_{22}]$ . In this way, one can obtain columns of  $[A]$  by performing the Gauss elimination and back substitution operations on the corresponding columns of  $[K_{21}]$ . The vector  $\{B\}$  is obtained in similar fashion by performing the Gauss elimination and back substitution operations on the vector  $[\Delta F_2]$ .

### 3.4 Determination of Stresses

The evaluation of the stress components (at the Gauss points of the elements) is done by the following stepwise procedure.

1. Calculate the relative deformation gradient  ${}^{t+\Delta t}_t\{F\}$  using equation (2.2): It should be noted that the position vector  ${}^t\mathbf{x}$  corresponds to the equilibrium position.
2. Decompose the relative deformation gradient as  ${}^{t+\Delta t}_t[F] = {}^{t+\Delta t}_t[R]{}^{t+\Delta t}_t[U]$  and determine  ${}^{t+\Delta t}_t[Q]$  and  ${}^{t+\Delta t}_t[U^p]$  using equation (2.4).
3. Determine the principal incremental logarithmic strain  ${}_t\{\Delta \epsilon^L\}$  using equation (2.15).
4. Calculate  ${}_t\{\Delta \sigma^M\}$  using equation (2.37). The integration of the constitutive equation is performed using the Euler forward technique described below.
5. Use equation (2.12) to calculate the Cauchy stress components at time  $t + \Delta t$ .

### 3.5 Integration of the Constitutive Equation

Different techniques exist for the integration of the constitutive equation (2.38). A simple and robust technique is the Euler forward integration scheme described below.

Assume that the principal incremental strain components have been calculated and the state of the Gauss point at time  $t$  is known.

If the state at time  $t$  is elastic,

1. Calculate the stress increment assuming elastic behavior:

$${}_t\{\Delta\sigma^M\} = [C^E]_t\{\Delta\varepsilon^L\}.$$

2. Calculate  ${}^{t+\Delta t}\{\sigma\}$  using (2.12).
3. Determine  ${}^t\sigma_{eq}$  and  ${}^{t+\Delta t}\sigma_{eq}$  using (2.20).
4. If  ${}^{t+\Delta t}\sigma_{eq} \leq {}^t\sigma_y$ , then elastic behavior holds, or if  ${}^{t+\Delta t}\sigma_{eq} = {}^t\sigma_{eq}$  the Gauss point is neutrally loaded. **Return.**
5. If  ${}^{t+\Delta t}\sigma_{eq} > {}^t\sigma_y$ , a transition from elastic to plastic has occurred. Calculate the

$$Ratio = \frac{({}^t\sigma_y - {}^t\sigma_{eq})}{({}^{t+\Delta t}\sigma_{eq} - {}^t\sigma_{eq})},$$

change the state to plastic and use the sub-incrementation method. In this method, the stress components with respect to the material frame are updated after each sub increment by the increment in stress components corresponding to the elasto-plastic strain sub increment. The  $[C^{EP}]$  corresponding to the last updated state is used:

$${}^{t+\Delta t}\{\sigma^M\}^{(i)} = {}^{t+\Delta t}\{\sigma^M\}^{(i-1)} + {}^{t+\Delta t}[C^{EP}]^{(i-1)} d_t\{\Delta\varepsilon^L\} \text{ for } i = 1, n$$

where

$$d_t\{\Delta\varepsilon^L\} = \frac{(1 - Ratio){}_t\{\Delta\varepsilon^L\}}{n},$$

$${}^{t+\Delta t}\{\sigma^M\}^{(0)} = {}^t\{\sigma^M\} + Ratio [C^E]_t\{\Delta\varepsilon^L\},$$

$${}^{t+\Delta t}\{C^{EP}\}^{(0)} = [C^{EP}] \text{ evaluated at } {}^{t+\Delta t}\{\sigma^M\}^{(0)}$$

Use equation (2.11) to find  ${}^{t+\Delta t}\sigma_{ij}$ . **Return.**

If the state at time  $t$  is plastic, the sub incrementation method described in (5) above is applied with ratio set to zero.

This describes the Euler forward integration scheme for the elasto-plastic model described in section 2.6.

## 3.6 Solution Procedure

Equation (3.35) represents only an approximate equilibrium equation at time  $t + \Delta t$  (the approximation is mostly due to the linearization and simplification involved in the steps between equations (2.49) and (2.50)). A solution of such an approximate equation may involve a significant amount of error and, depending on incremental displacement step, may become unstable. Therefore, it is necessary to modify equation (3.35) to turn it into an iterative problem capable of providing a solution with desirable accuracy. Amongst various iterative techniques, the modified Newton-Raphson algorithm is the most effective as it offers fast convergence with less computation. This algorithm is described in section 3.6.2.

As stated in section 1.2 of chapter 1, in the present problem, the friction at the punch-sheet interface is assumed to be sticking friction. The corresponding contact condition is applied only in an iterative fashion. Thus, there are two sets of iterations in the solution procedure of the present problem. First, for the specified incremental force/displacement, the contact iterations are carried out to determine the status (contact or non-contact) of the interface nodes. This algorithm is described in section 3.6.2. Then, corresponding to this status, modified Newton-Raphson iterations are carried out to minimize the error arising out of linearization and simplification of the equilibrium equation.

Numerical integration scheme for the elemental coefficient matrices and right side vectors and some divergence handling procedures for the modified Newton-Raphson scheme are presented in sections 3.6.3 and 3.6.4 respectively.

### 3.6.1 Contact Algorithm

This section describes the iterative procedure to apply the contact boundary conditions (2.52 and 2.53) to the linearized and condensed set of finite element equations (3.35). The iterative algorithm is as follows:

#### (I) First iteration:

1. In the first iteration, it is assumed that all the punch-interface nodes are sticking. Thus, the boundary condition given by the equation (2.52) is applied to all nodes.
2. Next these equations are solved to obtain  $\{_t\Delta u_1\}$ . The vector  $\{_t\Delta u_2\}$  is determined from equation (3.34). Thus, the whole incremental displacement vector  $\{_t\Delta u\}$  is known.
3. Then, the incremental reactions are found by multiplying the original coefficient matrix with the incremental displacement vector.
4. At the end of the contact iteration, the non contact nodes are identified using the condition  ${}^{t+\Delta t}F_z > 0$ .

#### (II) Second iteration:

1. Now the condition (2.53) is applied to all the non contact nodes.
2. Then the resulting equations are solved to find  $\{_t\Delta u_1\}$ . The vector  $\{_t\Delta u_2\}$  is found as before.
3. Now the reactions are found by the method described above.
4. Finally, a check is made to find whether any additional nodes are losing contact using the condition mentioned above.

#### (III) Further iterations:

The second step is repeated till there is no change in the contact status between two successive iterations.

### 3.6.2 Modified Newton - Raphson Scheme

The condensed set of approximate equilibrium equations (3.35), when the subscript/superscript denoting the time are restored, takes the form:

$${}^t[\widehat{K}]_t \{\Delta \widehat{u}\} = {}^t\{\Delta \widehat{F}\}. \quad (3.43)$$

The modified Newton-Raphson iterative scheme is used to convert this problem into an iterative problem to improve the accuracy of the solution. This algorithm can be stated as follows.

1. Form the FEM equation,

$${}^t[K]_t \{\Delta u\}^{(i)} = {}^{t+\Delta t}\{ERR\}^{(i-1)} \quad (3.44)$$

where

$${}^{t+\Delta t}\{ERR\}^{(i-1)} = {}^{t+\Delta t}\{F\}^{(i-1)} - {}^{t+\Delta t}\{f\}^{(i-1)}, \quad (3.45)$$

2. Get the condensed form of the equation 3.44,

$${}^t[\widehat{K}]_t \{\Delta \widehat{u}\}^{(i)} = {}^{t+\Delta t}\{\widehat{ERR}\}^{(i-1)} \quad (3.46)$$

3. Check for convergence given by the following criterion,

$$\frac{\|{}^{t+\Delta t}\{ERR\}^{(i)}\|}{\|{}^{t+\Delta t}\{F\}^{(i)}\|} \leq tol_c. \quad (3.47)$$

4. If not converged go to step 1.
5. If converged go to next increment.

The vector  ${}^{t+\Delta t}\{ERR\}$  is called the unbalanced force vector. The right superscript on  ${}^{t+\Delta t}\{F\}$  denotes the configuration on which the integration is to be performed for the external force vector. For first iterative step,

$${}^{t+\Delta t}\{ERR\}^{(0)} = {}^t\{\Delta F\} \quad (3.48)$$

### 3.6.3 Numerical Integration Scheme

Exact evaluation of integrals appearing in element coefficient matrices and right side vectors is not always possible because of the complexity of the integrand. In such cases, it is natural to seek numerical evaluation of these integral expressions. Numerical integration involves approximation of the integrand by a polynomial of appropriate degree, because the integral of a polynomial can be evaluated exactly.

The most commonly used numerical integration method is Gauss-Legendre integration method. The expression for the integral over a master element  $\Omega_R$  is given by

$$\begin{aligned} \int_{\Omega_R} F(\xi, \eta, \zeta) d\xi d\eta d\zeta &= \int_{-1}^{+1} \int_{-1}^{+1} \int_{-1}^{+1} F(\xi, \eta, \zeta) d\xi d\eta d\zeta \\ &\cong \sum_{i=1}^m \sum_{j=1}^n \sum_{k=1}^l F(\xi_i, \eta_j, \zeta_k) \omega_i \omega_j \omega_k \end{aligned} \quad (3.49)$$

where  $m$ ,  $n$  and  $l$  denote the number of quadrature points (Gauss-points) in  $\xi$ ,  $\eta$  and  $\zeta$  directions respectively and  $\omega_i$ ,  $\omega_j$  and  $\omega_k$  denote the corresponding weights. Two Gauss points in each direction are used in this work.

### 3.6.4 Divergence Handling Procedures

The modified Newton-Raphson method diverges in some cases. The following simple but fairly effective techniques, for overcoming the divergence, are incorporated in the present work.

1. **Line search:** When there is slow convergence or divergence in iterative step of an increment, the line search is invoked. In this, the right side vector of equation (3.44) is scaled by a factor  $\alpha_l$ . A number of values of  $\alpha_l$  in the range of ( $\alpha_{min}$  and  $\alpha_{max}$ ) are used. The value of  $\alpha_l$  corresponding to the minimum unbalanced force vector  ${}^{t\Delta t}ERR$  is used. Thus, instead of rejecting the whole iterative step, a compromise is made to reach the minima for the same iterative step. In the terms of the vector  ${}^{t\Delta t}ERR^i$  for  $i^{th}$  increment

$${}_l\{ERR\}^i \leq \alpha_l \{ERR\}^i : \alpha_{min} \leq \alpha_l \leq \alpha_{max} \quad (3.50)$$



2. **Incremental Cutting Method:** When the Modified Newton Raphson method is unable to converge within specified iterative steps, the whole increment is repeated. The increment is repeated with the reduced incremental step size. In the terms of the specified displacement, this condition can be stated as:

$$\{\Delta u^{specified}\}^i = \alpha_c \{\Delta u^{specified}\}^i, \quad \alpha_c < 1 \quad (3.51)$$

The Increment cutting method is computationally expensive and is used as a last resort.

# Chapter 4

## Results and Discussion

The finite element model of 3-dimensional deep drawing process developed in the previous chapter has been applied to a number of cases involving two materials (Aluminum-killed Steel and material in reference [19]) and various sets of process parameters to illustrate its applicability. The domain considered in section (2.8) of chapter 2 is discretized as shown in figure (4.1). Anticipating a stress concentration at the corner of the punch and in the clearance gap, the discretization is refined in these regions. The validation of the analysis is performed in section (4.1). The thickness strain distribution, deformed mesh and stress distribution for a typical case is discussed in section (4.2), (4.3) and (4.4). A parametric study is done in section (4.5) illustrating the effect of various parameters on punch-load and thickness strain.

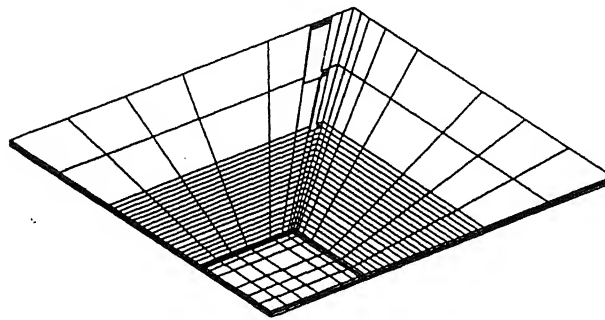


Figure 4.1: The Descretised Sheet

## 4.1 Validation

The fem code developed simulating the deep drawing process is validated with respect to experimental results given in reference [4]. The material used for this is aluminum-killed steel with physical properties and dimensions as follows:

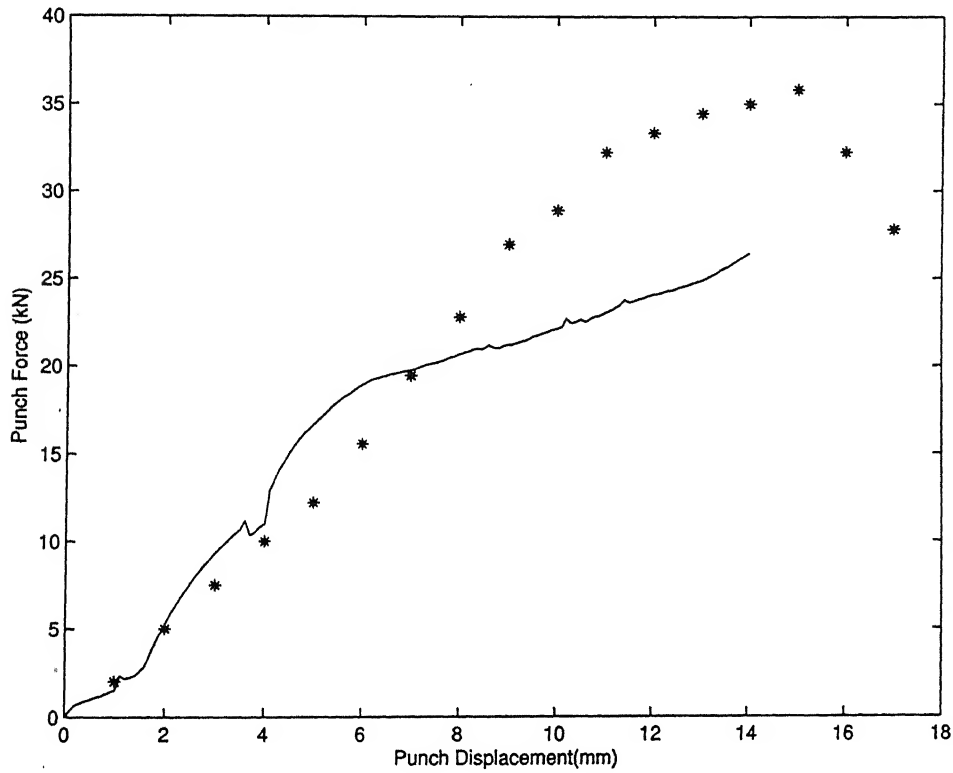


Figure 4.2: The variation of punch load with punch displacement

Material: Aluminum killed steel

Young's modulus  $E = 211.744$  Gpa,

Poisson's ratio  $\nu = 0.291$ ,

Initial Yield Stress  $(\sigma_y)_o = 172$  Mpa,

Hardening Coefficient  $K = 574.59$ ,

Hardening Exponent  $n = 0.269$ ;

Sheet dimensions (for domain shown in figure (2.4)):

Blank size  $s = 55 \text{ mm} \times 55 \text{ mm}$ ,

Punch size  $p = 20\text{mm} \times 20 \text{ mm}$ ,

Die size  $d = 21.25\text{mm} \times 21.25 \text{ mm}$ ,

Die radius  $r_d = 5\text{mm}$ ,

Punch radius  $r_p = 5\text{mm}$ ,

Corner radius  $r_c = 3.2\text{mm}$ ,

Sheet thickness  $t = 0.86\text{mm}$ ;

Blank holding force (for region shown in figure (2.5)) = 500 kg.

Figure (4.2) shows the variation of the punch load with the punch displacement for the above configuration. It can be seen that the punch-load follows closely with the experimental result for the initial deformation of the sheet till the punch radius region is in full contact with the punch after which there is a deviation in punch force from experimental values with increasing punch displacement. The reasons for the deviation may be as follows:

1. As reported in reference [4], at large punch displacements, the lubricant between the sheet and the die may be squeezed out due to which the coefficient of friction may not remain constant as assumed in the analysis. This may further affect the stress distribution and the deformation of the domain.
2. Due to limited computational resource and to limit the computational time, the meshing in the blank holder region is not refined. As these elements come under the deformation zone, stress developed may be higher than the actual value leading to higher punch load.

.1

## 4.2 Thickness Strain Distribution

Figures (4.3) show the thickness strain distribution in Aluminum killed steel sheet. The blank, punch and die sizes as well as blank holding force are the same as in section 4.1. In pure deep drawing process, the thickness of the sheet metal cannot change because the surface area does not change [2]. But, in actual practice, the thickness of drawn part varies considerably from the initial blank thickness.

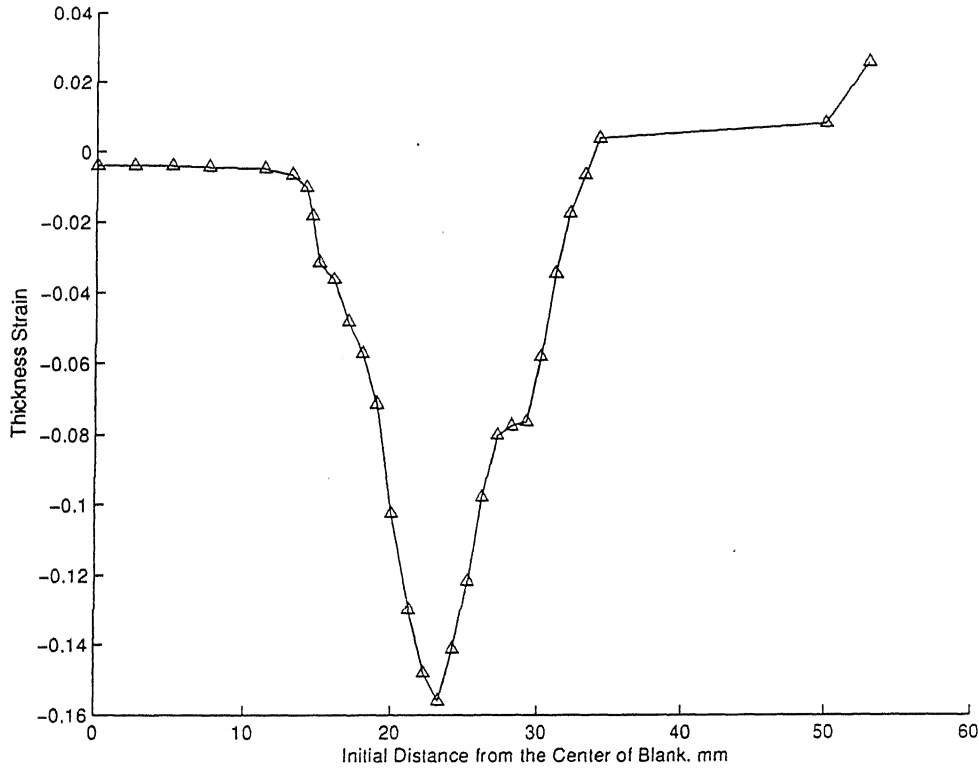


Figure 4.3: Thickness Strain of the sheet metal along the x axis

The thickness variation depends on the metal, the geometry of the formed part, and the drawing technique. The minimum thickness usually occurs within the curved portion of the part which connects the bottom with the walls. Figures (4.3) show that, as the draw depth is increased, the sheet is most severely stretched in the clearance space. The thickness of the sheet under punch is found to be less than the original thickness whereas, on the die it is slightly greater than the original thickness.

### 4.3 Deformed Mesh

Figure (4.4) shows the deformed mesh at the end of 14 mm of punch displacement.

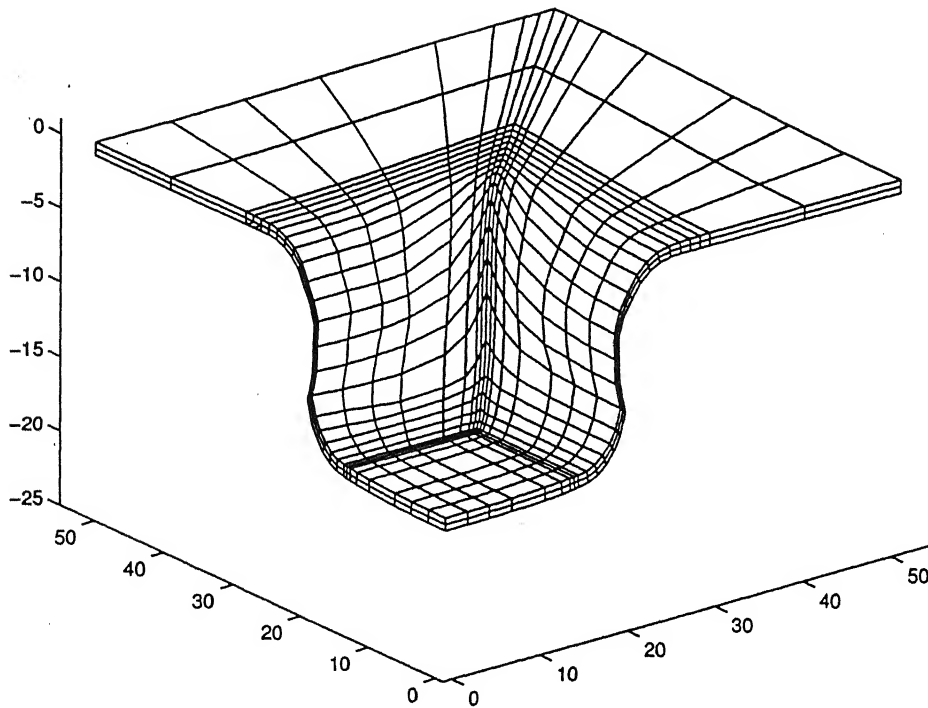


Figure 4.4: The deformed sheet metal

Aluminum killed steel sheet is used. The blank, punch and die sizes as well as blank holding force are the same as in section 4.1. The nodes in the punch radius region are considered to be sticking to the punch which is a fair assumption considering the large compressive force generated at the sheet-punch interface.

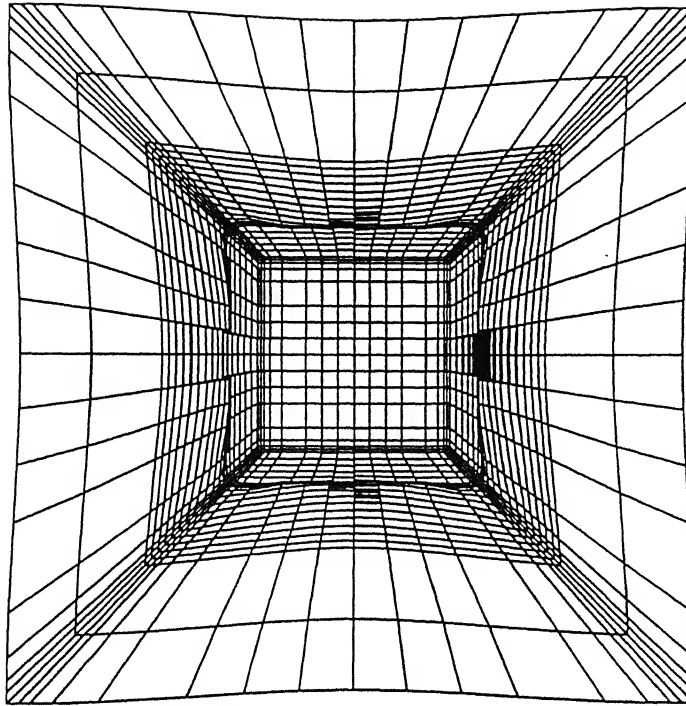


Figure 4.5: The complete plate showing ear formation at the corner

The top view for the whole sheet extrapolated from the one fourth portion of the sheet is shown in figure (4.5). The formation of ears can be seen at the corner of the plate. This phenomenon occurs due to the presence of extra materials. To avoid such kind of ear formation, the blank shape needs to be optimized.

## 4.4 Stress Distribution

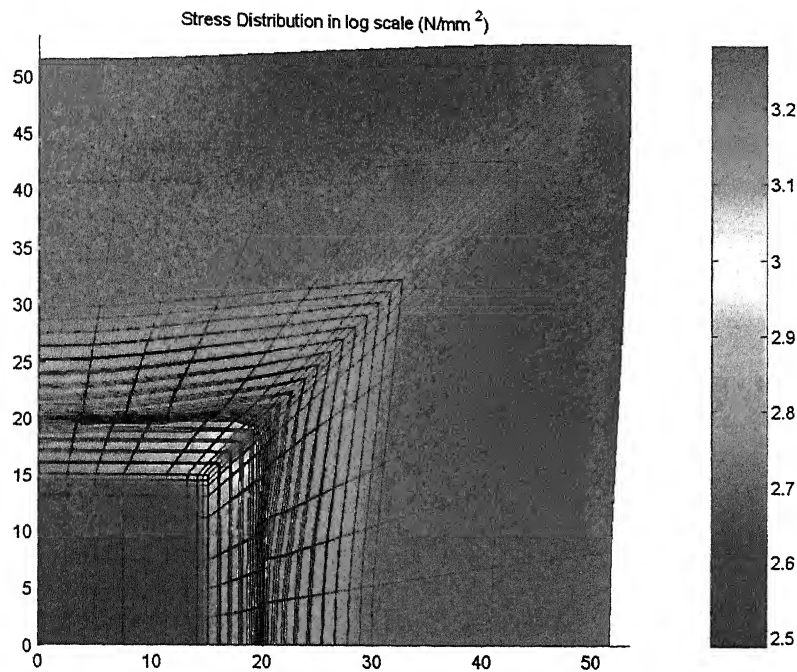


Figure 4.6: The Stress distribution in the domain

The equivalent stress distribution in the sheet during the deformation is shown in figure (4.6). It can be seen that the value of equivalent stress is maximum at the punch corner and from that point it decreased in all directions to reach a minimum at the sheet edges. The stress values are plotted in logarithmic scale.

## 4.5 Parametric Study

Various process parameters affect the final state of deformation and stress in the deep drawn cup. These may include sheet thickness, material properties, blank holder force, lubrication conditions between the sheet and die etc. The effect of some of these parameters is analyzed in the present work.

पुस्तकालय : विनायक कलकर पुस्तकालय  
भारतीय प्रौद्योगिकी संस्थान कानपुर  
अवधि क्र० A... 149280



#### 4.5.1 Effect of Sheet Thickness

The variation in punch load and thickness strain for different sheet thicknesses is studied in this section. The material property used and all other parameters are the same as in previous section. The effect of sheet thickness  $t$  on punch force is studied by carrying out the analysis for five cases ( $t = 0.50\text{mm}$ ,  $0.75\text{mm}$ ,  $0.86\text{mm}$ ,  $0.95\text{mm}$  and  $1.05\text{mm}$ ). Figure (4.7) shows the variation of punch force with punch displacement for these cases. It is observed that the punch force increases with the sheet thickness. Increase in the sheet thickness implies increase in the volume. Therefore, a large force is required to achieve the same punch displacement as shown in figure (4.7).

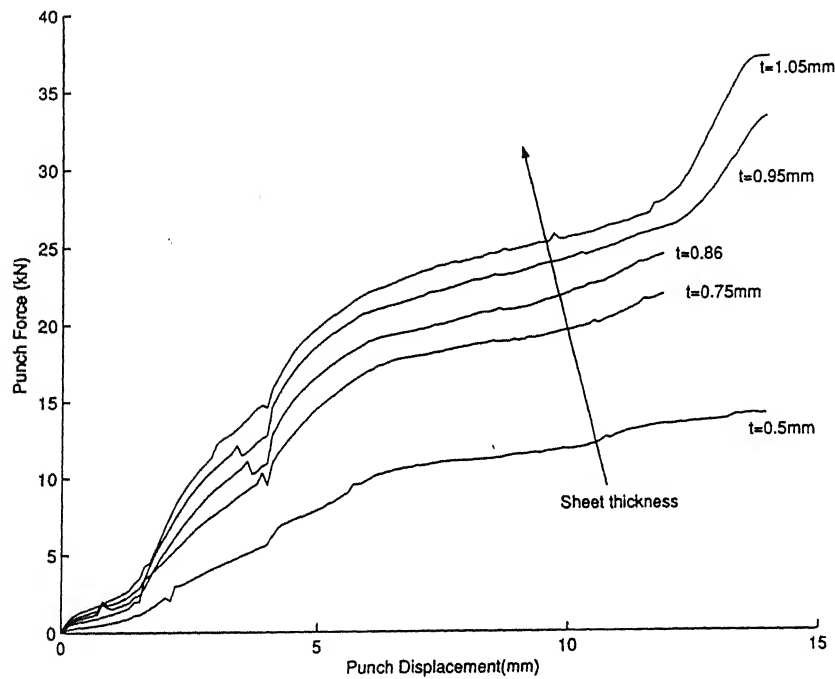


Figure 4.7: The variation of punch load with sheet thickness

Figure (4.8) illustrates the variation of thickness strain along one of the axis for different sheet thicknesses. No uniform variation in thickness is observed. However, maximum thickness strain increases with thickness.

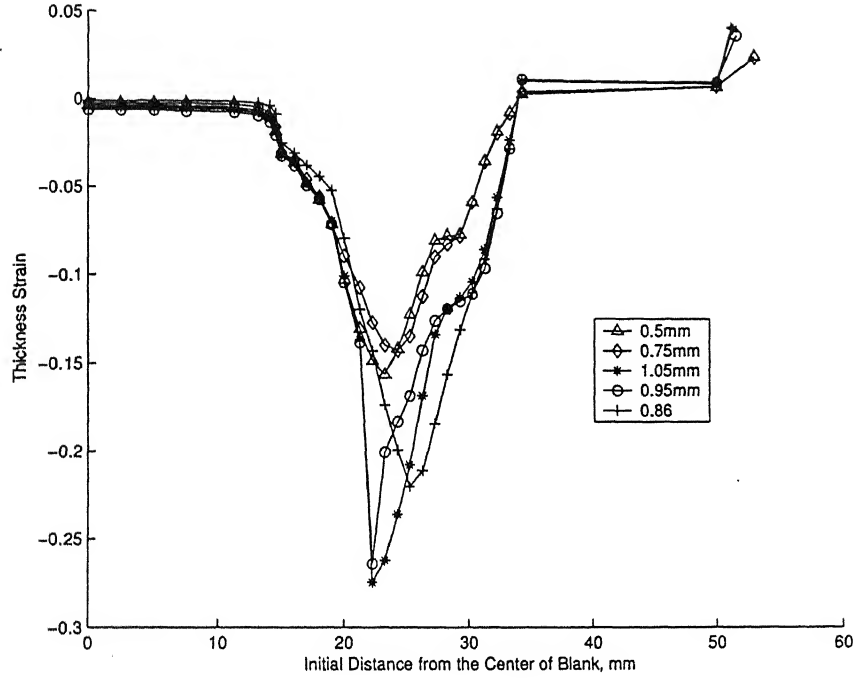


Figure 4.8: The variation of thickness strain with sheet thickness

#### 4.5.2 Effect of Material Properties

The punch force and thickness strain distribution are studied for one more material [19] the properties of which are as follows:

Material:

Young's modulus  $E = 71$  Gpa,

Poisson's ratio  $\nu = 0.33$ ,

Initial Yield Stress  $(\sigma_y)_o = 132.225$  Mpa,

Hardening Coefficient  $K = 444.45$  Mpa,

Hardening Exponent  $n = 0.52836$

The punch force and thickness strain of the sheet for this material are shown in figures (4.9) and (4.10). It can be seen that the trends in these figures are the same as for earliar material.

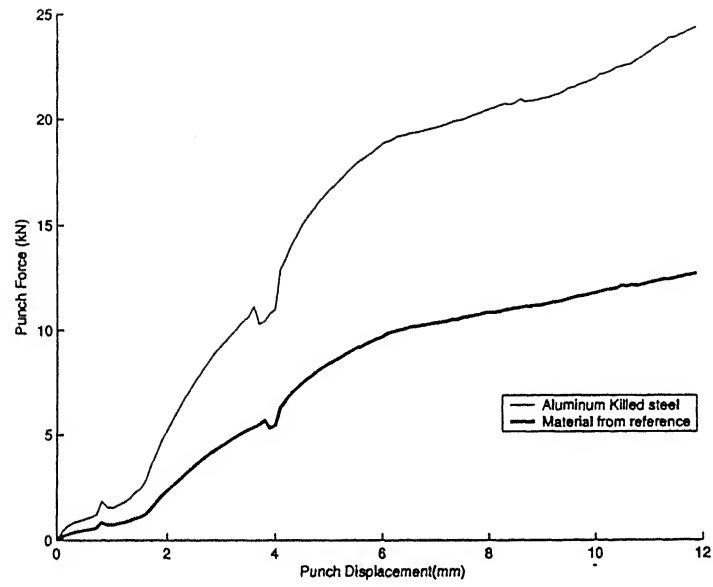


Figure 4.9: The variation of punch load with material

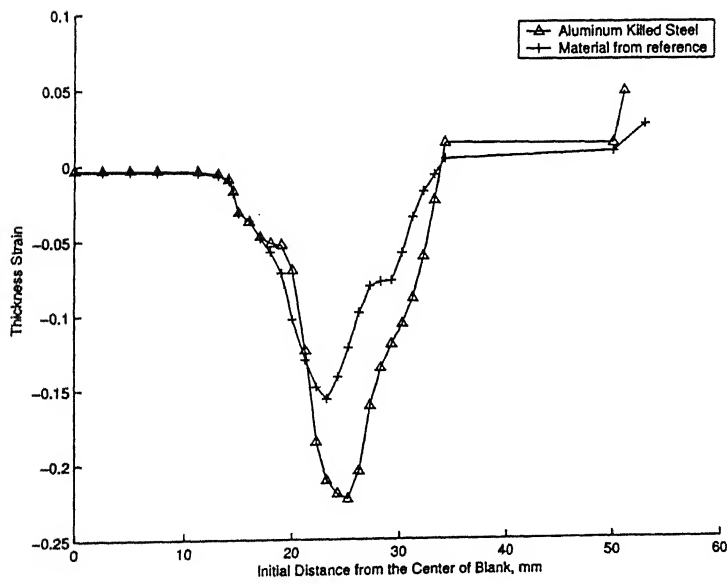


Figure 4.10: The variation of thickness strain with material

## Chapter 5

# Conclusions and Scope for Future Work

The deep drawing process is one of the most common manufacturing process for sheet metal parts. The nature of the deformation involved in this process and the complexity in describing the deformation mathematically, renders this process difficult to analyze and simulate.

A finite element simulation of deep drawing process using solid element is attempted. The incremental updated Lagrangian formulation is used with new incremental objective stress measure and logarithmic strain measure to formulate the mathematical framework for this simulation. Modified Newton-Raphson method is used to solve the resultant non-linear finite element equations. The material is assumed to be elastic-plastic strain hardening yielding according to von-Mises criterion. The strain hardening behavior is modeled by a power law. The inertial and body forces are neglected. The sticking friction is assumed at the punch-sheet interface and sliding friction is assumed at the sheet-die interface. The blank holding force is applied incrementally.

The validation of the finite element code, thus developed, is done with the available experimental results. The parametric study has been carried out to show the effect of two process variables namely, sheet thickness and material properties. The following conclusions are drawn from the analysis:

- The punch load it increases with the sheet thickness.

- Material properties have significant effect on the punch load. Higher punch load is required for the material with higher yield stress and larger hardening coefficient.
- The sheet thickness reduces at the clearance region owing to high tensile stress developing in the side wall of the drawn cup. This phenomenon manifests in the higher value of the thickness strain, which has a lower value in the clearance region.
- The equivalent stress developed in the sheet is the largest at the punch corner zone and reaches to a minimum value at the free edges of the sheet.
- For the drawing of square cup drawing from square blank, earring is observed.

This simulation of deep drawing process is based on many assumptions due to which the accurate representation of the process is still incomplete. The present work can thus be extended to the following:

- Most sheet metals exhibit anisotropy in their physical characteristics and it needs to be incorporated to describe the stress and strain variation.
- The present work assumes sticking friction at the punch-sheet interface. Sliding friction can therefore be included at this zone. Similarly, sliding friction can also be incorporated on the curved profiles of the punch and die.
- The present work can be extended to the deep drawing of arbitrary shape.
- Failure analysis of deep drawn parts in terms of wrinkling, earring, fracture etc. can be studied.
- Optimization of various process parameters such as blank-holder force, clearance gap, blank shape etc. can be included in the scope for further analysis.

# References

- [1] K. Lange, *Handbook of Metal forming*, McGraw-Hill Book Co., New York, 1985.
- [2] G. Schuler, *Metal Forming Handbook*, Springer-Verlag, Berlin, 1998.
- [3] G. Sachs, *Principles and Methods of Sheet Metal Fabricating*, Rein Hold Publishing Co., New York, 1966.
- [4] S. Kobayashi, S. Oh and T. Altan, *Metal Forming and The Finite Element Method*, Oxford University Press, Oxford, 1989.
- [5] C.H. Toh and S. Kobayashi, *Deformation Analysis and Blank Design in Square Cup Drawing*, Int. J. Mach. Tool Des. Res., 25, 15-32, 1985.
- [6] M.J. Saran, and A. Samulesson, *Elastic-Viscoplastic Implicit Formulation for Finite Element Simulation of Complex Sheet Forming Processes*, Int. J. Numer. Methods. Eng., 30, 1675-1697, 1990.
- [7] S.A. Majlessi, and D. Lee, *Deep Drawing of Square-Shaped Sheet Metal Parts, Part 1: Finite Element Analysis*, Trans ASME, J. Eng. Ind., 115, 102-109, 1993.
- [8] E. Onate, and C.A.D. Saracibar, *Finite Element Analysis of Sheet Metal Forming Problems using a Selective Viscous Bending/Membrane Formulation*, Int. J. Numer. Methods Eng., 30, 1577-1593, 1990.
- [9] C.H. Chou, J. Pan, and S.C. Tang, *Analysis of Sheet Metal Forming Operations by a Stress Resultant Constitutive Law*, Int. J. Numer. Methods Eng., 37, 717-735, 1994.
- [10] X. Shi, Y. Wei, and X. Ruan, *Simulation of Sheet Metal Forming by a One-Step Approach: Choice of Element*, J. Mat. Proc. Tech., 108, 300-306, 2001.

- [11] R. H. MacNeal, *Perspective on Finite Elements for Shell Analysis*, *Finite Elements Anal. Des.*, 30, 175-186, 1998.
- [12] C.H. Chou, J. Pan, and S.C. Tang, *An Anisotropic Stress Resultant Constitutive Law for Sheet Metal Forming*, *Int. J. Numer. Methods Eng.*, 39, 435-449, 1996.
- [13] P. Keck, M. Wilhelm, and K. Lange, *Application of Finite Element Method to The Simulation of Sheet Forming Processes: Comparison of Calculations and Experiments*, *Int. J. Numer. Methods Eng.*, 30, 1415-1430, 1990.
- [14] L.P. Lei, S.M. Hwang, and B.S. Kang, *Finite Element Analysis and Design in Stainless Steel Sheet Forming and its Experimental Comparison*, *J. Mat. Proc. Tech.*, 110, 70-77, 2001.
- [15] L. Kaiping, A. M. Habraken, and H. Bruneel, *Simulation of Square-Cup Deep-Drawing with Different Finite Elements*, *J. Mat. Proc. Tech.*, 50, 81-91, 1995.
- [16] P. Jetteur, *Non-Linear Shell Element Based on Maguerre Theory*, IREM Internal Report 85/5, Ecole Polytechnique Federale De Lausanne, Lausanne, December 1985.
- [17] A.G. Maimalis, D.E. Manolakos, and A.K. Baldoukas, *Simulation of Sheet Metal Forming using Explicit Finite Element Techniques: Effect of Material and Forming Characteristics, Part 2.: Deep Drawing of Square Cups*, *J. Mat. Proc. Tech.*, 72, 110-116, 1997.
- [18] J. Bonet, *Error Estimators and Enrichment Procedures for The Finite Element Analysis of Thin Sheet Large Deformation Process*, *Int. J. Numer. Methods Eng.*, 37, 1573-1591, 1994.
- [19] L.F. Menezes and C. Teodosiu, *Three Dimensional Numerical Simulation of Deep Drawing Process using Solid Finite Elements*, *J. Mat. Proc. Tech.*, 97, 100-106, 2000.
- [20] K. Osakada, C.C. Wang, and K.I. Mori, *Controlled FEM Simulation for Determining History of Blank Holding Force in Deep Drawing*, *Annals CIRP*, 44, 243-246, 1995.
- [21] M. Ahmetoglu, T.R. Broek, G. Kinzel, and T. Altan, *Control of Blankholder Force to Eliminate Wrinkling and Fracture in Deep-Drawing Rectangular Parts*, *Annals CIRP*, 44, 247-250, 1995.
- [22] R.D. Lorenzo, L. Fratini, and F. Micari, *Optimal Blankholder Force Path in Sheet Metal Forming Processes: An AI Based Procedure*, *Annals CIRP*, 48, 231-234, 1999.

- [23] Y.Q. Guo, J.L. Batoz, J.M. Detraux, and P. Duroux, *Finite Element Procedures for Strain Estimation of Sheet Metal Forming Parts*, Int. J. Numer. Methods Eng., 30, 1385-1401, 1990.
- [24] T.W. Ku, H.J. Lim, H.H. Choi, S.M. Hwang, and B.S. Kang, *Implementation of Backward Tracing Scheme of The FEM to Blank Design in Sheet Metal Forming*, J. Mat. Proc. Tech., 111, 90-97, 2001.
- [25] S.H. Kim and H. Huh, *Finite Element Inverse Analysis for the Design of Intermediate Dies in Multi-Stage Deep Drawing with Large Aspect Ratio*, J. Mat. Proc. Tech., 113, 779-785, 2001.
- [26] M. Colgan and J. Monaghan, *Deep Drawing Process: Analysis and Experiment*, J. Mat. Proc. Tech., 132, 35-41, 2003.
- [27] R. Roy, *A Primer on the Taguchi Method*, Society of Manufacturing Engineers, 1990.
- [28] R. Hill, *A Theory of the Yielding and Plastic Flow of Anisotropic Metals*, Proc. R. Soc. London, 193A, 281, 1948
- [29] J.W. Yoon, F. Barlat, R.E. Dick, K. Chung and T.J. Kang, *Plane Stress Yield Function for Aluminum Alloy Sheets- Part 2: FE Formulation and its Implementation*, Int. J. Plasticity, 20, 495-522, 2004
- [30] W. Hu and Z.R. Wang, *Anisotropic Characteristics of Materials and Basic Selecting Rules with Different Sheet Metal Forming Processes*, J. Mat. Proc. Tech., 127, 374-381, 2002
- [31] A.V. Hershey, *The Plasticity of an Isotropic Aggregate of Anisotropic Face Centered Cubic Crystals*, Trans. ASME J. Appl. Mech., 30, 241, 1954
- [32] M. Gotoh, *A Theory of Plastic Anisotropy based in a Yield Function of Fourth Order (Plane Stress State)*, Int. J. Mech. Sci., 19, 505, 1977
- [33] D. Banabic, T. Kuwabara, T. Balan, D.S. Comsa and D. Julean, *Non-quadratic Yield Criterion for Orthotropic Sheet Metals under Plane Stress Conditions*, Int. J. Mech. Sci., 45, 797-811, 2003
- [34] M. Itskov and N. Askel, *Plastic Anisotropy at Large Strains: Some Aspects of the Formulation of Orthotropic Yield Function*, Fifth World Congress on Computational Mechanics, Vienna, Austria, 2002



- [35] W.F Hosford, *A Generalized Isotropic Yield Criterion*, Trans. ASME J. Appl. Mech., 39, 607, 1972
- [36] F. Barlat, J.C.Brem and D.J.Lege, *A Six-component Yield Function for Anisotropic Materials.*, Int. J. Plasticity, 7, 693-712, 1991
- [37] A.P. Karafillis and M.C. Boyce, *A General Anisotropic Yield Criterion using Bounds and a Transformation Weighting Tensor*, J. Mech. Phys. Solids, 41, 1859-1886, 1993
- [38] F. Barlat, R.C. Becker, R.C. Hayashida, Y. Meada, M. Yanagawa, K. Chung, J.C. Brem, D.J. Lege, K. Matsui, S.J. Murtha and S. Hattori, *Yielding Description for Solution Strengthened Aluminum Alloy*, Int. J. Plasticity, 13, 385-401, 2003
- [39] F. Bron and J. Besson, *A Yield Function for Anisotropic Materials Application to Aluminum Alloys*, Int. J. Plasticity, 20, 937-963, 2004
- [40] M.Kawka and A.Makinouchi, *Plastic Anisotropy in FEM Analysis using Degenerated Solid Elements*, J. Mat Proc. Tech., 60, 239-242, 1996
- [41] H.C. Wu, *Anisotropic Plasticity for Sheet Metals using the Concept of Combined Isotropic-Kinematic Hardening*, Int. J. Plasticity, 18, 1661-1682, 2002
- [42] J.W. Yoon, I.S. Song, D.G. Yang, K. Chung and F. Barlat, *Finite Element Method for Sheet Forming based on an Anisotropic Strain-rate Potential and the Convected Coordinate System*, Int. J. Mech. Sci., 37, 733-752, 1995
- [43] E. Nakamachi, *Sheet Forming Process Charecterization by Static-Explicit Anisotropic Elastic-plastic Finite Element Simulation*, J. Mat. Proc. Tech, 50, 116-132, 1995
- [44] C. Truesdell, *The Elements of Continuum Mechanics*, Springer-Verlag, New York, 1966.
- [45] J.K. Dienes, *On The Analysis of Rotation and Stress Rate in Deforming Bodies*, Acta Mechanica, 32, 217-232, 1979.
- [46] D.P. Flanagan and L.M. Taylor, *An Accurate Numerical Algorithm for Stress Integration with Finite Rotations*, Comp. Methods Appl. Mech. Engg. 62, 305-320, 1987.
- [47] M.A. Crisfield, *Non linear Finite Element Analysis of Solids and Structures, 1,: Essentials*, John Wiley and Sons, Chichester, 1994.

- [48] D.R. Metzger and R.N. Dubey, *Objective Tensor Rates and Frame Indifferent Constitutive Models*, Mechanics Research Communications, 13(2), 91-96, 1986.
- [49] E.H. Lee, *Some Comments on Elastic-Plastic Analysis*, Int. J. Solids Struct., 17, 859-872, 1981.
- [50] D.R.J. Owen and E. Hinton, *Finite Elements in Plasticity: Theory and Practice*, Pineridge Press, Swansea, 1980.
- [51] K. J. Bathe, *Finite Element Procedures*, Prentice Hall of India, New Delhi , 1996
- [52] O.C. Zienkiewicz, *The Finite Element Method*, Tata McGraw-Hill Book Co., New Delhi, 1979.